This is a non-peer-reviewed preprint submitted to EarthArXiv.

This manuscript has been submitted for publication in Interpretation journal (https://pubs.geoscienceworld.org/interpretation).

Please note the manuscript has yet to be formally accepted for publication. Subsequent versions of this manuscript may have different content.

If accepted, the final version of this manuscript will be available via the 'Peer-reviewed Publication DOI' link on the right-hand side of this webpage.

The corresponding author of this manuscript is V. Antunes (vinicius.antunes@research.uwa.edu.au).

3D INVERSIONS OF MAGNETIC AND GRAVITY DATA FOR THE YAOURÉ REGION, IVORY COAST: A GREENSTONE BELT CHARACTERIZATION

Vinicius Antunes, Centre for Exploration Targeting, School of Earth and Oceans, The University of Western Australia, Crawley, WA, 6009, Australia. E-mail: vinicius.antunes@research.uwa.edu.au; ORCID: 0000-0002-4218-8852.

Vitaliy Ogarko, Centre for Exploration Targeting, School of Earth and Oceans, The University of Western Australia, Crawley, WA, 6009, Australia. E-mail: vitaliy.ogarko@uwa.edu.au; ORCID: 0000-0003-2487-109X.

Mark Jessell, Centre for Exploration Targeting, School of Earth and Oceans, The University of Western Australia, Crawley, WA, 6009, Australia. E-mail: mark.jessell@uwa.edu.au; ORCID: 0000-0002-0375-7311.

Jérémie Giraud, Centre for Exploration Targeting, School of Earth and Oceans, The University of Western Australia, Crawley, WA, 6009, Australia. GeoRessources, Université de Lorraine, CNRS, 54000 Nancy, France. E-mail: jeremie.giraud@uwa.edu.au; ORCID: 0000-0002-9100-4327.

Corresponding author: Vinicius Antunes, vinicius.antunes@research.uwa.edu.au

Keywords: 3D inversions, magnetics, gravity, greenstone belt.

Running head: 3D inversions of Yaouré greenstone belt

ABSTRACT

We carried out 3D inverse modeling of full tensor gravity gradiometry data, its derived products (T_z and T_z residual), and magnetic data to recover the density and magnetic susceptibility distributions of the Yaouré Greenstone Belt in Ivory Coast, West Africa. The study area presents significant challenges: it lacks well-defined stratigraphy and structural measurements, and it lies close to the magnetic equator, where the magnetic inclination is low. Inverted models were analyzed using isosurfaces and histogram curves to characterize physical properties distribution and highlight geophysical sources. We extracted vertical slices through the 3D inverted models across significant mapped structures and lithotypes, and measured magnetic anomaly dips within these sections to create an artificial structural map. We identified positive and negative density contrasts as well as magnetic susceptibility sources in the region that correlated with mapped surface geology. Our results revealed that sedimentary and volcano-sedimentary rocks in the region present higher susceptibility than some intrusions, contrasting with their comparatively lower density. The 3D inverted models provided insights of some mapped structures, such as major faults, that may act as physical property boundaries. Ranking magnetic susceptibility and density contrast of geological units alongside the structural map offers a systematic first approach to maximizing the value of geophysical inversions. This integration may serve as a petrophysical or geological constraint when prior information is limited for subsequent inversions, acting as useful information for starting or reference models.

INTRODUCTION

Greenstone belts have received considerable attention for decades due to their economic potential. These successions comprise important assets for mineralization, as they are often

linked with various commodities and are considered the principal rock type in Precambrian cratons to host orogenic gold and may act as source terrains for sedimentary gold (Ridley, 2013). This is particularly evident in the West African Craton (WAC), where major orebodies are found within its Paleoproterozoic domain, currently the largest Paleoproterozoic gold-producing province globally (Goldfarb et al., 2017; Masurel et al., 2022).

Despite the importance of greenstone belts in this province, several studies have relied on analyzing geophysical data sets using 2D or 2.75D forward models (Baratoux et al., 2011; Jessell et al., 2012; Perrouty et al., 2012; McFarlane et al., 2019), without fully exploiting modern computational capacity to produce comprehensive 3D inversions models that can depict physical property distributions more accurately, with the exception of Martin et al. (2013).

The inversion of geophysical data sets allows the expansion of the "search space" to include the subsurface in regions that may lack large outcropping bodies, thus improving the geological mapping for mineral exploration as it retrieves geometric and physical property distributions of the subsurface. In addition, inverse modeling is valuable when the relationship between gridded geophysical data and geological model not straightforward, as is often the case for greenstone sequences since they present folding, thrusting, and greenschist-facies metamorphism (Condie, 1981; Gill, 2010; Anhaeusser, 2014).

The widespread availability and relatively low-cost acquisition of magnetic and gravity data have driven rapid advances in 3D inversion techniques using these data sets (Blum et al., 2000; Silvennoinen and Kozlovskaya, 2007; Gallardo and Thebaud, 2012; Wang et al., 2012; Giraud et al., 2019; Eshaghi et al., 2023). Such developments have enabled the characterization of density and magnetic susceptibility within greenstone sequences, thereby facilitating mineral

resource exploration and improving the geological understanding of these units, whose origin and even definition remain subjects of debate (Anhaeusser, 2014).

In this paper, we present the geophysical investigation of a Proterozoic greenstone belt through the inversion of airborne magnetic and full tensor gravity gradiometry (FTGG) data. The Yaouré Greenstone Belt (YGB), situated within the southern WAC (sWAC), serves as the case study for this work. We carried out 3D inversions of the data set to characterize the distribution of magnetic susceptibility and density within the belt. By integrating these results with a geological map, we derived an artificial structural map and a physical property table for the region.

GEOLOGIC SETTING

Located in central Ivory Coast, the YGB is the eastern portion of the Bouaflé Greenstone Belt, being part of the Paleoproterozoic Baoulé-Mossi Domain in the sWAC (Grenholm et al., 2019). This part of the craton encompasses the Man-Leo Shield, which is divided into two domains, i.e., an Archean basement called Kénéma-Man domain and a Paleoproterozoic one (also known as Birimian terrane) named Baoulé-Mossi (Perret et al., 2025 and references therein). While the Kénéma-Man Domain crops out in Guinea, Sierra Leone, Liberia, and Ivory Coast, and is associated with high-pressure metamorphism of amphibolite and granulite facies, the Baoulé-Mossi - presented in Guinea, Senegal, Burkina Faso, Ghana, Togo, Ivory Coast, and Mali – has an intermediate-pressure type metamorphism of greenschist and amphibolite facies (Cahen and Snelling, 1984).

The Baoulé-Mossi Domain is comprised of elongate belts of volcanic, volcano-sedimentary, and sedimentary rocks divided by sedimentary basins and granitoid rocks, and it hosts the majority of Au, porphyry Cu, Pb-Zn, and sedimentary Mn Paleoproterozoic deposits in the West African Craton (Markwitz et al., 2016; Masurel et al., 2022). The greenstone belts presented in this domain have undergone accretion to the Archean Leo-Man craton and subsequent metamorphism to greenschist facies (Perret et al., 2025). These rocks were affected by the ~2 Ga Eburnean orogeny (Eglinger et al., 2017), which is a term used for the Paleoproterozoic thermal and tectonic events that have affected the West African Craton (Pouclet et al., 2006). This orogeny was characterized globally by the continental collision between the San Francisco and Congo cratons and locally in the sWAC by the collision between the Kénéma-Man and Baoulé-Mossi domains (Weber et al., 2016; Grenholm et al., 2019).

The YGB (Figure 1a), i.e., the eastern portion of the Bouaflé Greenstone Belt, is located near the southern part of the Kossou Lake in central Ivory Coast. It hosts the ~1.5 Moz Yaouré gold deposit, along with several artisanal mining sites situated to the south of the region (Ngom et al., 2022). The deposit lies away from the region's major fault zones, except for two significant structures: the Koudougou-Benou fault, with trends northeast-southwest, and the Tokorossou-Benou fault, whose strike changes from east-west to northeast-southwest toward the east.

The Yaouré mine has been studied recently from a tectono-stratigraphic perspective by Mériaud et al. (2022) using different analyses such as geological mapping, core logging, 3D modeling, interpretation of geophysical data, lithogeochemistry, and radiogenic isotope analyses. Two main sequences were reported for the mine site (Figure 1b): a lower basaltic sequence and

an upper volcano-sedimentary sequence. The basaltic sequence comprises massive basalts and well-preserved, undeformed pillow basalts. It is crosscut by granodiorites, quartz-feldspar porphyries, hornblende porphyries, and nepheline-bearing diorites. This basaltic sequence has no thickness reported. The volcano-sedimentary sequence, approximately 300-m thick and exposed north of the deposit, consists of an andesitic mass flow (50 to 60-m thick) overlain by homogeneous dacites (~250-m thick). The andesitic unit is crosscut by hornblende porphyry dykes, and both units are intruded by ~5 m-thick nepheline-bearing diorite dykes.

METHODS

Geophysical survey

Airborne survey data, acquired by Bell Geospace for Perseus Mining in 2021, included magnetic and FTGG measurements. The survey used 100 m flight line spacing (NS orientation) with an average terrain clearance of 80 m covering an irregularly shaped area of approximately 468 km^2 (see Figure 1a). No tie lines were flown for this survey. The elevation within the study area ranges from 150 to 600 m (Figure 2), with the highest terrain occurring in the central-southern sector, corresponding to the Mount Yaouré hills. More details of the survey are found in Table 1.

Data processing

Magnetic data

The Total Magnetic Intensity (TMI) data were provided with standard reductions already applied, e.g., diurnal correction, spike removal, leveling correction, etc. (Milsom and Eriksen,

2011; Dentith and Mudge, 2014). The inclination and declination for the region at the time of the survey were -13º and -4.2º, respectively. The International Geomagnetic Reference Field (IGRF) reported for the area is 32118.3 nT. We performed the inversion using TMI data directly, assuming induced magnetization only. Additionally, magnetic data modeling best practices recommend minimal filtering operations to preserve data integrity and achieve optimal results (Li, 2008). The inversion algorithm's capability to process TMI data directly further supported this choice.

In this study, the regional magnetic field was removed by subtracting the arithmetic mean of the TMI data, i.e., 32077.85 nT. In addition, fine-tuning the mean value between -100 nT and 100 nT through inversions showed that a mean shift of -20 nT yields the best correspondence with the regional field, indicated by a cleaner removal of non-anomalous signal. Therefore, the final value subtracted from the TMI data was 32057.85 nT, and the resulting data set is hereafter referred to Total Magnetic Anomaly (TMA).

To downsample the data, originally sampled every 6 m along flight lines, a minimum curvature interpolation (Briggs, 1974; Swain, 1976; Webring, 1981) with a grid cell size of 100 m was applied using the Oasis Montaj suite (Seequent Limited, 2023). The resulting data set for inversion comprises 49,735 data points out of the original 792,870, each at the center of a grid cell in the XY plane and then assigned an altitude specified by the Altitude field of the survey. This field corresponds to the sensor height recorded during acquisition. The observed data grid can be seen in Figure 3.

FTGG, T_z, and T_z residual data

The FTGG data comprises the five independent components of the gravity gradient tensor or the second derivatives of the gravity potential in the x, y, and z directions of a Cartesian coordinate system, i.e., T_{xx}, T_{yy}, T_{xy}, T_{yz}, and T_{xz}, along with the dependent second vertical derivative, i.e., T_{zz}, which is equal to $-(T_{xx} + T_{yy})$ due to Laplace's equation (Blakely, 1995). Each individual component, or any combination of components, can be gridded and employed to investigate an area from distinct viewpoints; for example, the T_{xx} component is effective for delineating north-south-trending structures due to its ability to resolve east-west variations, whereas accurately T_{zz} typically produces a more intuitive representation of the anomaly field (Martinez et al., 2013; Pilkington, 2014). Among the individual components, T_{zz} captures the most primary features in inversion, but incorporating additional components into the inversion progressively improves resolution and delineation of target features (Martinez et al., 2013).

This method provides greater sensitivity to edges and lateral contrasts, offering improved resolution for distinguishing closely spaced anomalies compared with conventional gravimeter surveys that measure only the vertical component, T_z (Paoletti et al., 2016; Meng et al., 2024). As gravity gradiometer measures variations in the gravitational acceleration, the constant background level associated with whole earth effects is already removed in the acquisition. In addition, the FTGG data does not require latitude, free-air, or Bouguer corrections, as these effects are usually below the measurement noise (Dransfield, 1994).

The FTGG data underwent proprietary processing by Bell Geospace, beginning with noise reduction applied to the leveled free-air data, where a cutoff wavelength of 200 m was applied. Subsequently, a proprietary terrain correction, which is required for FTGG data, was applied to this noise-reduced data set. A bulk rock density of 2,200 kg/m^3 was assumed for

terrain correction (C. Murphy, 2021, Bell Geospace, Internal Report), as the highest ridges of the central mountain located in the south-central portion of the area have a laterite cap (Figure 2). This density correction value demonstrated to be optimal for these features, as densities above 2,200 kg/m^3 may overcorrect the ridges and produce a low gravity response over them, whereas densities below this value leave some residual terrain highs (S. J. Lowe, 2021, Southern Geoscience Consultants, Internal Report).

The gravity vertical anomaly (T_z), derived from the terrain-corrected FTGG tensor components, was also used as the data set for the inversions. Inversions were performed on both T_z and its residual, referred to here as T_z Res. The T_z Res represents the signal obtained after applying a high-pass Butterworth filter (10 km cutoff) to T_z, thereby retaining the high-frequency components. It is important to note that T_z does not contain the very long-wavelength trends typically observed in conventional gravity surveys, as it was calculated directly from the tensor components (Christopher Bellamy, personal communication, 2024).

All the FTGG and derived data were downsampled using the interpolation and gridding parameters as described for the magnetic data set, resulting in 49,735 data points out of the original 79,211. The grids described here in this section are shown in Figure 4.

Model grid design

The 3D core model grid used for the inversions consisted of 100 x 100 x 100 m cells. The number of core cells in the easting, northing, and elevation were 231 (N_x), 263 (N_y), and 20 (N_z), respectively, covering an area of approximately 23 km x 26 km x 2 km (easting, northing, and depth). This cell size was selected for the core area to achieve a balance between the

computational costs and the camp-scale of the survey area, i.e., situated between 300 and 3000 km^2 (McCuaig, 2017), as the scope of this research is to investigate the larger geological features of the region.

A padding of 5 km was added on each side of the core area – east, west, north, and south – resulting in a total horizontal padding of 10 km in the easting and northing directions. Vertically, 8 km in the vertical direction was added using padded cells. The padded cells have an expanding factor of 1.15 in all directions. That is, the cell size progressively increases from the core area toward the edges of the 3D model grid. The 10 km depth was chosen because greenstone belts have been reported to have this maximum thickness from gravity interpretations (Losier, 1986). We therefore added 38, 38, and 18 padded cells in the easting, northing, and depth directions, respectively. Padding may prevent edge effects for anomalies located near the borders of the core area. Furthermore, the use of larger cells reduces the total number of cells, thus decreasing both inversion runtime and memory requirements without significant loss of detail for the study area (Williams, 2008). The expanding factor of 1.15 was found to be to be optimal in this study, as it reduced the model array by about 40 times with a reasonable inversion result. Larger expanding factors could lead to stratification artifacts (Ogarko et al., 2024). The final flat model grid consisted of 269 x 301 x 38 cells (N_x, N_y, N_z), extending around 43 km (easting), 43 km (northing), and 10 km (depth).

Topography was added into the final flat-topped model grid by shifting the columns of the model so that the top layer of cells followed the elevation derived from four Radiometrically Terrain Corrected (RTC) images from the Advanced Land Observing Satellite – Phase Array type L-band Synthetic Aperture Radar, ALOS PALSAR (ASF DAAC, 2014), which were

merged for the study area. These images consisted of high-resolution terrain corrected products with 12.5 m resolution. The images are merged and then clipped to match the extent of the final flat model grid. The translation of the ALOS PALSAR data onto the model grid was performed using the Rasterio Python library (Gillies and Others, 2013).

Inversion parameters

We performed 3D inversions using the Tomofast-x 2.0 package (Giraud et al., 2021; Ogarko et al., 2024) for both the magnetic and FTGG data. This free and open-source software, written in Fortran 2008 standard, can run on shared memory and CPU clusters. Due to this and the fact that our model grid and data set are for a camp to regional scale (49,735 data points × 3,076,822 cells), we ran this software on The University of Western Australia's Kaya High Performance Computing facility. The computer node used consisted of Intel Xeon Gold 6254 36 processors and 382 GB of RAM.

For all inversions performed in this study, the following settings have been applied: distance weighting constraint and matrix wavelet compression. Distance weighting (Li and Oldenburg, 2000) is a type of mathematical constraint more indicated for when topography and/or borehole were present as it considers not only the vertical variations in the data but also horizontal ones to minimize the natural decay of potential fields and thus enabling all cells to have equal chance to contain sources (Williams, 2008). The second feature involves the wavelet compression of the sensitivity matrix (Li and Oldenburg, 2003), where the compression rate, implemented in Tomofast-x (Martin et al., 2013; Ogarko et al., 2024), is linearly proportional to the RAM usage. A wavelet compression rate of 0.05 using a Haar wavelet was applied, i.e., the matrix retained 5% of its original size, allowing a decrease of the sensitivity matrix by a factor of

200 (Ogarko et al., 2024). Although a strong compression rate was used in the inversions, no significant degradation of the model structure was observed due to the scale of the problem, thus enabling each inversion to be performed using reduced RAM usage.

Despite diamagnetic materials occurring in nature, e.g., quartz and feldspar (Temnikova et al., 2025), their magnetic susceptibility is so weak or even negative that they are considered non-magnetic and cannot be detected on geophysical surveys (Dentith and Mudge, 2014). Therefore, the use of positivity, i.e., 'forcing' the inversion to retrieve values of apparent magnetic susceptibility equal to or above zero, is recommended. In addition, positivity may bring a correct dip and a depth to the top of the anomalous source (Li and Oldenburg, 1996). We have used the disjoint interval bound constraint, DIBC (Ogarko et al., 2021), to apply positivity in the inversion of the magnetic data from zero to unity.

DIBC has been successfully applied to constrain inversions in a variety of geological settings, such as mineralized Proterozoic basement (Rashidifard et al., 2024), mountain chains (Martin et al., 2025), and sub-ice shelf regions (Bird et al., 2025). This constraint involves determining multiple interval bounds for the retrieved property, either for individual model grid cells or for the entire model, using the alternating direction method of multipliers, ADMM (Boyd et al., 2011 and references therein). A global bound of 0 to 1 (SI unit) was chosen based on the relatively weak TMA response and the assumption that the rocks presented in the study area, i.e., mafic, felsic volcanics, and volcaniclastics, have magnetic susceptibilities below 1 SI according to literature values (Clark and Emerson, 1991; Hunt et al., 1995; Schön, 2015). The DIBC also allows the use of a dynamic ADMM weight where this term is multiplied by an ADMM weight

factor whenever the data misfit falls below a user-defined threshold. A data cost threshold of 0.003 was defined based on experimentation with several inversion tests.

The inverted model based on the FTGG components was applied with a power of three (cubic) distance weighting constraint because, unlike gravity field data (e.g., T_z and T_z residual), these measurements decay with the cube of the distance from the source, similarly to the magnetic field decay.

A target misfit of 7×10^{-9} s^{-2} (7 E) was selected empirically, as the noise level is situated around this value. For the T_z and T_z residual data sets, a model target misfit of 10^{-7} m/s^2 (0.01 mGal) was adopted to recover the density contrast.

More information about the inversions, such as data misfit grids, reconstruction error and RAM for all the models can be seen in Appendix A.

Geological correlation and dipping of anomalies

The 3D inverted models were clipped to the core area, i.e., the geophysical survey extent, and analyzed using isosurfaces and depth slices using the ParaView software (Ahrens et al., 2005). These features were examined in relation to the geological units and structures shown in Figure 1a. It is important to notice that the Bouaflé Greenstone Belt geological map was derived from field observations and interpretation of aeromagnetic maps (Mériaud, 2020). Consequently, some units were mapped according to their magnetic signature, e.g., high magnetite granodiorite and low magnetite granodiorite units. Nevertheless, this map represents the most up-to-date interpretation available and, therefore, it was used as the geological reference for our analysis.

Isosurfaces for the density models were selected using extreme percentiles (i.e., the 2.5th and 97.5th percentiles) to display the lowest- and highest-density sources. Although the density models showed similarly shaped histograms that approximate a normal distribution, they do not strictly follow a Gaussian distribution. Therefore, the use of percentile-based thresholds provided a more robust criterion. For the magnetic susceptibility model, the 97.5th percentile (0.043 SI) was used as a reference threshold. Nevertheless, isosurfaces at this value produced geobodies with unrealistically deep roots so we decided to adopt a slightly higher cutoff (0.05 SI) to better constrain the geometry and improved consistency with the mapped geology.

Depth slices of inverted models were extracted from the 3D full models using the ParaView software (Ahrens et al., 2005) along directions perpendicular to the two main faults in the study area, i.e., the Koudougou-Benou (KB) and Tokorossou-Benou (TB) faults, named after the villages they intersect, as well as through the central portion of the survey. These 2D slices provide better detail to visualize structures and allow for more accurate measurements of the dip and dip direction of key anomalies. We have measured anomalies only in the magnetic susceptibility model, as magnetic data have been more extensively applied than gravity data to delineate depth, geometry, and orientation of sources (Cooper, 2006, 2014; Subrahmanyam and Rao, 2009).

The measurement of strike and dip of anomalies from 2D slices can support the development of petrophysical models using implicit modeling, as such methods require a structural database. A note of caution is due here since our measurements constitute an artificial structural data set derived from inversions. Nevertheless, these measurements can be associated with geological features, providing an initial framework for building a geological or

petrophysical model that can subsequently serve as a starting or prior model in further inversions. We suggest that this feedback approach, i.e., quantifying inverted models into structural data to feed subsequent inversion runs, can be particularly useful in areas with limited structural information and scarcity of outcrops, such as the Yaouré region.

The workflow was carried out in ParaView. We have applied ten equidistant contour levels in each slide to highlight some subtle anomalies. Two points situated at the anomaly of interest were selected to define a line contained in the slice plane. Dip direction and dip angle were then computed with a Python script using Euclidean geometry functions in 3D space.

Propagation of uncertainty was calculated considering horizontal and vertical uncertainties related to core model cell size, i.e. 100 m. The uncertainty formulation is explained more fully in Appendix B.

RESULTS AND DISCUSSION

To analyze the distribution of magnetic susceptibility and density across the study area, we present key features from the inverted models along with depth slices perpendicular to the main geological features, i.e., major faults and large mapped geological bodies. In addition, source bodies that do not correlate with any geological feature are highlighted.

It is important to note that the models discussed here can be considered unconstrained despite a few constraints have been applied to them, e.g., distance weighting and positivity (the latter applied only to the magnetic susceptibility models). As a result, they are subject to interpretation ambiguity due to the inherent non-uniqueness of the inverse problem. The use of unconstrained inversions, however, is a common practice in mineral exploration (Oldenburg and

Pratt, 2017), as it allows for an initial assessment of subsurface structures without imposing prior geological or petrophysical bias.

Overview of inverted models with mapped geology

Both magnetic susceptibility and density models show only moderate contrasts in the recovered properties. We also note that there is no overlapping of high positive nor high negative density contrasts with high magnetic susceptibilities, suggesting no strong correlation for these properties. Nevertheless, several subtle but significant anomalies can be identified on the inverted models and are described below.

The magnetic susceptibility model retrieved from the TMA data (Figure 5a) showed a range of 0 to 0.24 (SI units). The model also contained values slightly below zero, with a minimum of -2.2×10^{-15} SI, despite the application of positivity through the DIBC constraint. This is expected, as floating-point arithmetic of computers can accumulate round-off errors for operations used in the inversion software, such as matrix multiplications and iterative solvers. Therefore, negative values were not considered in the model. Three orders of magnitude spanned from the model, i.e., from 10^{-3} to 10^{-1} SI (Figure 5e), with majority of susceptibilities situated around 10^{-3} to 10^{-2} SI. These values, 10^{-3} to 10^{-1} SI, are within the range of magnetic susceptibilities reported in the literature for rock types similar to those present in the study area, such as basalts and granodiorites, situated from 10^{-3} to 10^{-1} SI (Clark and Emerson, 1991; Dentith and Mudge, 2014) and volcaniclastics, 11.18×10^{-4} to 1.18×10^{-2} SI (Lenhardt et al., 2013) and 10^{-3} to 25×10^{-3} SI (Nitzsche et al., 2006). These literature values are provided as general reference from physical property tables and are not measurements from the study area itself.

Density contrast values from the inverted model ranged mostly between -200 and 200 kg/m^3 for the FTGG, T_z, and T_z residual data sets (Figure 5b, c, and d). The density contrast distributions (Figure 5f) indicate that model values are centered around zero density contrast, with the T_z residual data model showing the smallest standard deviation, followed by the T_z and FTGG models.

The FTGG-derived model (Figure 5b) showed density contrast values ranging from -295 to 299 kg/m^3, following an approximately normal distribution centered around zero but relatively broad, indicating higher standard deviation and variance, with most values between -200 and 200 kg/m^3. The T_z-derived model (Figure 5c) ranged from -398 to 1144 kg/m^3 and also exhibited a near-normal distribution centered around zero, though less dispersed, with the majority of values between -100 and 100 kg/m^3. The T_z residual-derived model (Figure 5d) ranged from -228 to 474 kg/m^3 and displayed a similar normal-like distribution centered around zero, where most density contrast values are situated within -50 to 50 kg/m^3.

Analysis of the mapped geology alongside with the isosurfaces derived from values of and slightly above the 97.5th percentile of the inverted models revealed two principal domains separated by the NE-oriented KB fault: one characterized by high magnetic susceptibilities and the other by both high positive and negative density contrast values. These domains are hereafter referred to as the northern and southern domains, respectively.

The northern domain hosts most of the high magnetic susceptibilities, extending from the surface to depths of approximately 2,000 m. These sources (Figure 5a) are mostly situated within the volcano-sedimentary unit, followed by the sedimentary rocks. This distribution is somewhat expected, as these units are mostly represented by low anomalies in the TMA data (Figure 3).

Such behavior is consistent with the fact that, in regions of low magnetic inclination, magnetic sources typically generate negative anomalies (Nettleton, 1962). We also observed that there is a lack of high magnetic sources beneath the high-magnetite granodiorite unit in the northern domain, whereas such sources occur beneath the equivalent unit in the southern domain, suggesting distinct magnetic properties between them. Another interesting feature is that the magnetic source bodies within the northern domain are mainly located in a northeast-southwest trend aligned with the also northeast-southwest strike of the volcano-sedimentary unit. This includes the deepest magnetic source, located west of the northern mapped high magnetite granodiorite, which extends to depths exceeding 4 km and may represent a deeper root of the nearby granodiorite body.

Regarding density contrast, the northern domain showed no significant deviations from the background density. Moreover, the absence of low-density zones and the presence of a few high magnetic sources in the sedimentary unit differ from results reported in the literature, i.e., sedimentary units display both low magnetic susceptibility and low density (Enkin et al., 2020). This discrepancy may indicate the presence of small, unmapped intrusive bodies within the region.

The southern domain is characterized by having fewer high magnetic bodies compared to the northern domain. Magnetic sources are identified within the volcano-sedimentary unit north of the Yaouré mine, the high mag intrusion (mafic) unit, and the granodiorite unit in the southern region. The mafic intrusion near the KB fault appears to be magnetic, whereas equivalent units elsewhere in that domain showed weaker susceptibility responses, suggesting a lower content of magnetite. Moreover, the geometry and position of the sources associated with the high

magnetite granodiorite unit in the southern region did not entirely correlate with the mapped geological surface.

In the southern domain, both high negative (given by the 2.5th percentile value) and high positive density contrasts (given by the 97.5th percentile value) are situated almost entirely in the basalt unit, with sources located between the surface and approximately 1 km depth. The inverted models showed deeper density sources in the FTGG-derived model, followed by those from the T_z and T_z residual data (Figure 5b, c, and d, respectively). A possible explanation for this might be the progressive attenuation or removal of longer wavelengths from the original FTGG data to derive T_z, and subsequently the high-pass filtering inherent in the T_z residual. All three density inverted models presented more positive than negative density contrasts. These positive density contrasts are mostly associated with the high mag intrusion (mafic) unit, suggesting that denser sources within the basalt unit may indicate unmapped mafic intrusions or denser basaltic material. The latter could correspond to massive basalt flows with fewer vesicles (Moore, 2001; Gill, 2010), as the study area has an alternation between massive and pillow basalts.

No significant density or magnetic susceptibility contrasts were observed in the mine area within the discretized mesh. A finer mesh, e.g., with cell sizes of around 25 m, could potentially identify smaller anomalies. However, this was beyond the scope of the present study, as reducing mesh size would substantially increase computational demands, and we are focusing on a camp-scale area. An interesting feature, nevertheless, is a positive density source located immediately east of the Yaouré deposit. This body, approximately 1 km thick, may be related to the

intercepted granodiorite at about 800 m depth in a drill hole, previously detected in a seismic data set (Ralph and Saunders, 2023).

Characterization of anomalies in vertical slices

The vertical slices were grouped into three sets of figures (Figure 6, 7, and 8), each displaying three profiles that integrate the four inverted models with the mapped geology. We focused on the analysis of the magnetic susceptibility and the grouped FTGG-, T_z-, and T_z residual-derived density models, as these three density models exhibit broadly similar structure patterns, thus not requiring an exhaustive analysis. However, we highlighted key differences in those three density models where relevant.

We have classified our magnetic anomaly dips into four categories: low angle (0-30°), medium angle (30-60°), high angle (60-80°), and very high angle (80-90°). This classification provides a more consistent framework for analysis, accounting for variations in dip measurements caused by the irregular geometry of the anomalies. Although we referred to these measurements as structural data, no kinematic interpretation is implied, as the intent is solely to quantify the orientation of the identified features.

Each profile description begins with the main structural element, either the KB or TB fault, followed by the discussion of the most significant features along the profile, progressing from the magnetic susceptibility to the density models.

Slices perpendicular to the KB fault

Profile R-R’ (Figure 6), located in the northern segment of the KB fault, revealed no significant contrast in either the magnetic susceptibility or density models (Figure 6b, c, d, and e) across this structure. Two magnetic sources have been measured (Figure 6b) dipping to the southeast at high angles. The first source, situated between the contact of the sedimentary rock and the high magnetite granodiorite, displayed a susceptibility of approximately 0.06 SI, suggesting a possible extension of the granodiorite eastward, dipping southeast. The second measured anomaly, located close to the TB fault but not oriented perpendicular to it, also exhibited high angle dip, although susceptibility is lower, suggesting that features south of this fault may dip toward the east-southeast. A third anomaly, located at around 20 km along the profile, was associated with the high mag intrusion (mafic) unit, which has a northeast strike. This anomaly dips at a high angle to the southeast and coincides with a high negative density contrast in the density slices (Figure 6c, d, and e).

The susceptibility section from profile S-S’ (Figure 6f) displayed a background susceptibility for the KB fault. Nevertheless, this structure separates a positive density contrast on the left-hand side from a negative one on the right-hand side (Figure 6g, h, and i). This is most evident in the FTGG-derived density model (Figure 6g), where both anomalies extend to greater depths than those observed in the other density slices (Figure 6h and i). A moderately high magnetic source occurs within the volcano-sedimentary unit, dipping at a high angle to the southeast, consistent with its counterpart along profile R-R’ profile. The central mafic intrusion is associated with a high susceptibility source (around 0.08 SI) dipping southeastward and with an estimated thickness of about 1 km. This depth is consistent with the density models (Figure 6g, h, and i), which showed a high positive density contrast anomaly at the same location and depth. A high negative density contrast was identified at approximately 20 km along the profile

within the basalt unit, suggesting a relatively lower content of mafic minerals in this area compared to other parts of the same unit.

The T-T' profile displayed moderately high susceptibility dips to the southeast beneath the KB fault (Figure 6j). However, a note of caution is due here since a deeper anomaly in the same region exhibits an opposite dip direction, and thus the near-surface anomaly may not be directly associated with the fault structure. The volcano-sedimentary unit showed localized zones with high susceptibilities, possibly indicating the presence of unmapped intrusions, especially as this unit is divided into positive and negative density contrast regions (Figure 7k and m). At approximately the 8 km mark of the profile, the late calc-alkaline unit displays a relatively high susceptibility (~0.04 SI), whereas the equivalent intrusion at around the 16 km mark showed no significant magnetic response, despite both exhibiting positive density contrasts. This suggests that these units possess distinct magnetic properties. Toward the end of the profile, the mafic unit displayed high angle dip to the southeast and a high negative density contrast, consistent with the mafic unit intersected along the R-R' profile. This may indicate that the mafic bodies in the southeastern portion of the study area display a different geophysical signature compared to those in the central region.

Slices perpendicular to the TB fault

The TB fault along the U-U' profile (Figure 7) acts as a boundary between two distinct magnetic anomalies. The anomaly north of the fault (i.e., around the 7 km mark) can be associated with the sedimentary rock unit, and it is characterized by a very high angle towards north, with both greater size and intensity compared to the anomaly south of the fault. The southern anomaly, in contrast, displayed a moderate dip toward the south and is likely related to

the low magnetite granodiorite unit. The volcano-sedimentary unit showed some high susceptibility values, while the southern low magnetite granodiorite unit displayed the highest susceptibilities along the section, suggesting that the low magnetite granodiorite south of the KB fault may be more magnetic than its northern equivalent. A positive density contrast source could be seen in the FTGG-derived slice (Figure 7c), i.e., around the 14 km mark, within the volcano-sedimentary unit, followed by a transition to a negative contrast approaching the KB fault. This pattern of a positive to negative density contrast toward the KB fault can also be seen in the S-S' and T-T' profiles of the KB fault slices (Figure 6h and l).

Along the V-V' profile, the TB fault showed no significant susceptibility anomaly. However, a high negative density contrast occurs beneath it (Figure 7g, h, and i), but it can also be attributed to the sedimentary rock unit. This unit is associated with a high magnetic source (~0.07 SI) dipping northward, while the calc-alkaline and mafic intrusion units also displayed a high susceptibility, but dipping southward. A high positive contrast is observed immediately south of the KB fault (~16 km mark), corresponding to the basalt unit, followed by a negative contrast linked to the low mag granodiorite in the southern end of the profile.

In the W-W' profile, the TB fault acts as a boundary between two magnetic sources (Figure 7j): the northern anomaly is associated with the sedimentary unit, whereas the southern one is related to the mafic unit, with each dipping in opposite directions. The basalt unit did not display any magnetic contrast despite showing small positive density sources (less than 1 km deep) near the 17 km and 20 km marks along the profile (Figure 7k, l, and m). These features may indicate the presence of non-magnetic intrusions within the basalt unit or just localized zones of higher density.

Slices of the central area

Three additional slices were analyzed to encompass areas not covered by the previous slices, with their orientations selected to intersect a broad range of lithotypes.

The X-X' profile, oriented parallel to the easting axis, showed a small-sized high susceptibility source associated with the mafic unit in the 10 km mark (Figure 8b). This source has an estimated thickness of 800 m to 1,500 m if we consider the weaker anomaly surrounding the main source. A moderately high susceptibility anomaly with a medium-angle dip eastward and a top depth of around 1 km is associated with the volcano-sedimentary unit. A subtle, weak magnetic source dipping westward may be associated with the Yaouré mine. Nevertheless, due to the scale of the models used in this work, it was not possible to define the possible lithotypes associated with that source. The density slices (Figure 8c, d, and e) highlighted the highest positive density contrast observed in the 97.5th percentile-based isosurfaces (Figure 5b, c, and d), located east of the Yaouré mine and likely associated with the granodiorite intercepted by a drill hole (Ralph and Saunders, 2023). This source extends from roughly 1 km to 2 km depth with a density contrast of approximately 260 kg/m^3, suggesting that the granodiorite has a distinct geophysical signature compared to its low- and high-magnetite equivalents.

The Y-Y' profile, oriented along a northeast-southwest trend, intersects five of the seven lithotypes in the study area. The unmapped region in the northeastern portion is probably due to the presence of the man-made Lake Kossou. Within this profile, the volcano-sedimentary unit exhibited a high-angle magnetic source dipping northeastward, whereas the basalts and low magnetite granodiorite units dip toward the southwest (Figure 8f). The density models (Figure 8g, h, and i) displayed a correlation between density contrast and lithotypes, i.e., there is an

alternance of positive and negative contrasts coinciding with lithotype changes. For instance, two main positive density sources correspond to the mafic intrusion and to the basalt or late calc-alkaline unit, while the volcano-sedimentary unit and northern basalt are characterized by negative contrasts.

The north-south oriented Z-Z' profile intersects all the lithotypes except the low magnetite granodiorite and the late calc-alkaline intrusion. The high magnetite granodiorite unit can be associated with two high susceptibility anomalies, both dipping towards to the south (Figure 8j). The northern anomaly (around 6 km mark in the profile) dips at a high angle, whereas the southern one exhibits a low to moderate angle. The southern anomaly is considerably smaller than the mapped granodiorite body, suggesting that the inversion in this region may require additional constraints to improve resolution. The density contrast slices (Figures 8k, l, and m) revealed positive contrasts beneath the mafic intrusions, along with a broader and deeper anomaly below the basalt unit around the 20 km mark, suggesting that the mafic intrusion may extend to greater depths in this area, forming a large-wavelength anomaly indicative of a deeper magmatic root.

Overview of physical properties and magnetic dipping map

Based on the preceding analyses, a ranking of magnetic susceptibility and density was established for the geological units in the study area (Table 2). A note of caution is due here since we are presenting average values derived from the inverted models. However, local variations in the order may occur, as physical properties can vary substantially within the same geological unit due to differences in fabrics, structure, and mineralogy (Dentith and Mudge, 2014).

Magnetic susceptibility appears to correlate more consistently with geological units than density, i.e., we have six and four ranks for each property, respectively. The high mag intrusion (mafic) is the only unit that share the same rank in both properties, being the highest in each category. This suggests that in poorly mapped portions of the study area and surroundings, the coincident occurrence of high susceptibility together with a high positive density contrast can be used as an indicator of mafic intrusion where lithotype classifications are uncertain. Late calc-alkaline intrusions could not be reliably distinguished in the inverted models, being grouped with basalts. This is probably due to the relatively small size of these units when compared to the mesh cell dimensions. A closer inspection of the table indicates that basalts exhibit lower susceptibility than the volcano-sedimentary and sedimentary units. It is difficult to explain this result, but it may reflect variable magnetite content in volcano-sedimentary and sedimentary within greenstone belts, which can range from iron-rich to more magnetite-poor compositions (Stettler et al., 1997). In addition, pyroclastics (a subset of volcaniclastics) for the region are reported to contain lithic fragments rich in magnetite, while the sedimentary unit includes conglomerates with chert clasts containing hematite or magnetite and matrix with detrital magnetite (Mériaud et al., 2020).

The dip and dip direction estimates derived from the magnetic susceptibility slices (Figures 6, 7, and 8) allowed us to construct a magnetic dip map (Figure 9). Overall, the area is characterized predominantly by high angle dips, particularly within the sedimentary and mafic intrusions, whereas medium to low angle dips were observed for the low magnetite granodiorite and the basalt units. It is important to acknowledge the interpretational ambiguities inherent in this analysis, as several anomalies displayed irregular geometries, thus making the determination of dip direction and angle uncertain. In addition, petrophysical properties may not always

correlate directly to lithotypes, adding further uncertainty in the interpretation. However, we think this workflow provides a valuable first-order geological and petrophysical framework that can serve as a starting or reference model for subsequent geophysical inversions. This approach is especially useful for geological modeling techniques that employ implicit methods, i.e., geological surfaces are represented as iso-values of a 3D scalar field, which typically require structural and stratigraphical data as input (Wellmann and Caumon, 2018; de la Varga et al., 2019; Grose et al., 2021). Therefore, extracting quantitative information from geophysical inversion results, even when not fully constrained, represents an important step toward developing more realistic and geologically consistent 3D models.

CONCLUSION

We have generated inverted models using FTGG data, its derived products, and magnetic data, and developed an integrated interpretation based on isosurfaces and slices from the 3D inverted models. This approach enabled the extraction of geologically meaningful information from a challenging setting, i.e., a geological area characterized by limited structural and stratigraphy data, as well as a low magnetic inclination. Our methodology provided an initial framework for analyzing 3D inverted models to image the spatial distribution of magnetic susceptibility and density of a greenstone belt, subsequently enabling the construction of a petrophysical chart ranking the relative physical properties of the geological units presented in the study area. Furthermore, the quantitative assessment of magnetic anomalies into an artificial structural map offered a first step to feed inversion packages with petrophysical models and thereby improved subsurface interpretations. The results also provided new insights into the geology and geophysical signatures of the study area, revealing interesting features that may

represent potential exploration targets and validating structures described in previous information, e.g., the intrusion east of Yaouré mine identified in the density models. In addition, the qualitative and quantitative assessment of physical properties via 3D inversions may offer an additional procedure of clarifying differences between greenstones, which are still not fully understood. We believe this workflow has the potential to be applied in different greenstone belts in the West African Craton and other similar settings to maximize the value of geophysical inversions as it can refine or better constrain pre-existing geological models.

ACKNOWLEDGMENTS

V. Antunes would like to acknowledge Perseus Mining for providing the airborne survey data used in this study and permission to publish the results. This research forms part of a PhD project undertaken at The University of Western Australia (UWA), where V. Antunes was supported by a University International Fee Scholarship and a University Postgraduate Award. Partial funding for travel for PhD project itself was provided by AMIRA Global, the industry sponsors, and geological surveys, that composed the West African Exploration Initiative (WAXI), phase 4 - series P934C. We acknowledge the support of the Mineral Exploration Cooperative Research Centre (MinEx CRC) and the Loop consortia (LP170100985 and LP210301239). The work has been supported by the MinEx CRC, whose activities are funded by the Australian Government's Cooperative Research Centre Programme. This publication is MinEx CRC document 2026/018.

J. Giraud acknowledges support from the Australian Research Council through the Early Career Industry Fellowship grant no. IE240100281.

The authors also acknowledge the use of Kaya, the High-Performance Computing facility at UWA, for running the inversions presented in this work. We also thank Elizabeth Bruce, Taige Liu, and Kim Frankcombe for their support in the inversions.

APPENDIX A

SUPPLEMENTARY INFORMATION ABOUT INVERSIONS

Figure A-1 and A-2 display the observed, calculated and data misfit (i.e., observed – calculated) grids for the all the inversions discussed in this work.

Table A-1 displays the RAM usage, runtime, and the reconstruction error for all the inversions performed in this study. The reconstruction error measures how much the compressed sensitivity matrix differs from the original one and it is given by the output variable called compression error in Tomofast-x.

APPENDIX B

DIP ANGLE UNCERTAINTY

From the two endpoints that define the line where a magnetic anomaly was measured, we can define by Euclidean distance the vertical distance, V, and the horizontal distance, H. The measured dip angle, θ, is given by:

$$\theta = arctan\left(\frac{V}{H}\right) \text{ (rad)} \qquad (B-1)$$

We have treated both distances as independent positional uncertainties, δV and δH, where the location of a given measured point can be off to up to max of half a cell size, c, given by

$$\delta V = \delta H = \frac{c}{2}. \qquad (B-2)$$

Computing the partial derivative of θ (equation B-1) with respect to V and H using chain rule:

$$\frac{\partial \theta}{\partial V} = \frac{H}{H^2 + V^2}. \qquad (B-4)$$

$$\frac{\partial \theta}{\partial H} = \frac{-V}{H^2 + V^2}. \qquad (B-5)$$

Using the law of propagation of uncertainty, it gives us:

$$\delta\theta = \sqrt{\left(\frac{\partial \theta}{\partial V}\right)^2 \delta V^2 + \left(\frac{\partial \theta}{\partial H}\right)^2 \delta H^2}. \qquad (B-6)$$

Replacing the partial derivatives, equations B-4 and B-5, into the uncertainty propagation formula, equation B-6:

$$\delta\theta = \sqrt{\left(\frac{H}{H^2 + V^2}\right)^2 \delta V^2 + \left(\frac{-V}{H^2 + V^2}\right)^2 \delta H^2}. \qquad (B-7)$$

Then, $\delta\theta$ is converted from radians to degrees for representation.

In the following, we present a practical example focusing on the magnetic anomaly 1, as shown in Figure 5b. We defined a line along the anomaly using two endpoints specified by their 3D Cartesian coordinates (x, y, z):

Point 1: (x, y, z) = (215000, 783668, -297.08)

Point 2: (x, y, z) = (215168, 783500, -985.32)

To calculate the measured dip angle, θ, we compute the vertical distance, V, and the horizontal distance, H, and then insert those values into equation B-1:

$$\theta = arctan\left(\frac{688.24}{237.59}\right) \approx 1.24 \text{ (rad)} \approx 71°.$$

The cell size for the core area is 100 m. Substituting this value into the positional uncertainty terms, δV and δH, in equation B-2 yields:

$$\delta V = \delta H = \frac{100}{2} = 50\, m.$$

Replacing the positional uncertainties into the uncertainty propagation formula, equation B-7:

$$\delta\theta = \sqrt{\left(\frac{688.24}{(688.24^2 + 237.59^2)}\right)^2 50^2 + \left(\frac{-237.59}{688.24^2 + 237.59^2}\right)^2 50^2} \approx \pm 0.07\ (rad) \approx \pm 4°.$$

The result for the dip angle and its associated uncertainty is $71° \pm 4°$.

REFERENCES

Ahrens, J., B. Geveci, and C. Law, 2005, ParaView: An End-User Tool for Large-Data Visualization, *in* C. D. Hansen and C. R. Johnson, eds., Visualization Handbook, Butterworth-Heinemann, 717–731.

Anhaeusser, C. R., 2014, Archaean greenstone belts and associated granitic rocks – A review: Journal of African Earth Sciences, **100**, 684–732, doi: 10.1016/j.jafrearsci.2014.07.019.

ASF DAAC, 2014, ALOS PALSAR High Resolution Radiometric Terrain Corrected Product: NASA Alaska Satellite Facility Distributed Active Archive Center, doi: 10.5067/Z97HFCNKR6VA.

Baratoux, L., V. Metelka, S. Naba, M. W. Jessell, M. Grégoire, and J. Ganne, 2011, Juvenile Paleoproterozoic crust evolution during the Eburnean orogeny (~2.2–2.0Ga), western Burkina Faso: Precambrian Research, **191**, 18–45, doi: 10.1016/j.precamres.2011.08.010.

Bird, L. A., V. Ogarko, L. Ailleres, L. Grose, J. Giraud, F. S. McCormack, D. E. Gwyther, J. L. Roberts, R. S. Jones, and A. N. Mackintosh, 2025, Gravity-derived Antarctic bathymetry using the Tomofast-x open-source code: a case study of Vincennes Bay: The Cryosphere, **19**, 3355–3380, doi: 10.5194/tc-19-3355-2025.

Blakely, R. J., 1995, Potential Theory in Gravity and Magnetic Applications: Cambridge University Press.

Blum, M. L. B., A. C. B. Pires, and R. A. V. de Moraes, 2000, Gravity inversion on granite-greenstone belt areas: Crixás, Guarinos and Pilar de Goiás, Brazil: Brazilian Journal of Geology, **30**, 547–550, doi: 10.25249/0375-7536.2000303547550.

Boyd, S., N. Parikh, E. Chu, B. Peleato, and J. Eckstein, 2011, Distributed Optimization and Statistical Learning via the Alternating Direction Method of Multipliers: Foundations and Trends® in Machine Learning, **3**, 1–122, doi: 10.1561/2200000016.

Briggs, I. C., 1974, Machine contouring using minimum curvature: Geophysics, **39**, 39–48, doi: 10.1190/1.1440410.

Cahen, L., and N. J. Snelling, 1984, The Geochronology and Evolution of Africa: Clarendon Press Oxford.

Clark, D. A., and J. B. Emerson, 1991, Notes On Rock Magnetization Characteristics In Applied Geophysical Studies: Exploration Geophysics, **22**, 547–555, doi: 10.1071/EG991547.

Condie, K. C., 1981, Archean Greenstone Belts, 1st ed.: Elsevier Scientific Pub. Co.

Cooper, G. R. J., 2006, Obtaining dip and susceptibility information from Euler deconvolution using the Hough transform: Computers & Geosciences, **32**, 1592–1599, doi: 10.1016/j.cageo.2006.02.019.

Cooper, G. R. J., 2014, The automatic determination of the location, depth, and dip of contacts from aeromagnetic data: Geophysics, **79**, J35–J41, doi: 10.1190/geo2013-0181.1.

Dentith, M. C., and S. T. Mudge, 2014, Geophysics for the Mineral Exploration Geoscientist: Cambridge University Press.

Dransfield, M. H., 1994, Airborne Gravity Gradiometry: PhD Thesis, The University of Western Australia.

Eglinger, A., N. Thébaud, A. Zeh, J. Davis, J. Miller, L. A. Parra-Avila, R. Loucks, C. McCuaig, and E. Belousova, 2017, New insights into the crustal growth of the Paleoproterozoic margin of the Archean Kéména-Man domain, West African craton (Guinea): Implications for gold mineral system: Precambrian Research, **292**, 258–289, doi: 10.1016/j.precamres.2016.11.012.

Enkin, R. J., T. S. Hamilton, and W. A. Morris, 2020, The Henkel Petrophysical Plot: Mineralogy and Lithology From Physical Properties: Geochemistry, Geophysics, Geosystems, **21**, 1–26, doi: 10.1029/2019GC008818.

Eshaghi, E., R. Vayavur, R. S. Smith, C. Mancuso, F. D. Justina, and J. Ayer, 2023, Density and magnetic susceptibility of major rock types within the Abitibi greenstone belt: a compilation with examples of its use in constraining inversion: Exploration Geophysics, **54**, 647–669, doi: 10.1080/08123985.2023.2236154.

Gallardo, L. A., and N. Thebaud, 2012, New insights into Archean granite-greenstone architecture through joint gravity and magnetic inversion: Geology, **40**, 215–218, doi: 10.1130/G32817.1.

Gill, R., 2010, Igneous Rocks and Processes: A Practical Guide: Wiley.

Gillies, S. and Others, 2013, Rasterio: geospatial raster I/O for Python programmers. Available at: https://github.com/rasterio/rasterio.

Giraud, J., V. Ogarko, R. Martin, M. Jessell, and M. Lindsay, 2021, Structural, petrophysical, and geological constraints in potential field inversion using the Tomofast-x v1.0 open-source code: Geoscientific Model Development, **14**, 6681–6709, doi: 10.5194/gmd-14-6681-2021.

Giraud, J., M. Lindsay, V. Ogarko, M. Jessell, R. Martin, and E. Pakyuz-Charrier, 2019, Integration of geoscientific uncertainty into geophysical inversion by means of local gradient regularization: Solid Earth, **10**, 193–210, doi: 10.5194/se-10-193-2019.

Goldfarb, R. J., A.-S. André-Mayer, S. M. Jowitt, and G. M. Mudd, 2017, West Africa: The World's Premier Paleoproterozoic Gold Province*: Economic Geology, **112**, 123–143, doi: 10.2113/econgeo.112.1.123.

Grenholm, M., M. Jessell, and N. Thébaud, 2019, A geodynamic model for the Paleoproterozoic (ca. 2.27–1.96 Ga) Birimian Orogen of the southern West African Craton – Insights into an evolving accretionary-collisional orogenic system: Earth-Science Reviews, **192**, 138–193, doi: 10.1016/j.earscirev.2019.02.006.

Grose, L., L. Ailleres, G. Laurent, and M. Jessell, 2021, LoopStructural 1.0: time-aware geological modelling: Geoscientific Model Development, **14**, 3915–3937, doi: 10.5194/gmd-14-3915-2021.

Hunt, C. P., B. M. Moskowitz, and S. K. Banerjee, 1995, Magnetic Properties of Rocks and Minerals, *in* T. J. Ahrens, ed., Rock Physics & Phase Relations, American Geophysical Union, 189–204.

Jessell, M. W., P. O. Amponsah, L. Baratoux, D. K. Asiedu, G. K. Loh, and J. Ganne, 2012, Crustal-scale transcurrent shearing in the Paleoproterozoic Sefwi-Sunyani-Comoé region, West Africa: Precambrian Research, **212–213**, 155–168, doi: 10.1016/j.precamres.2012.04.015.

Lenhardt, N., H. Böhnel, M. Hinderer, and J. Hornung, 2013, Paleocurrent direction measurements in a volcanic setting by means of anisotropy of magnetic susceptibility: A case study from the Lower Miocene Tepoztlán Formation (Transmexican Volcanic Belt, Central Mexico): Sedimentary Geology, **290**, 1–14, doi: 10.1016/j.sedgeo.2013.02.013.

Li, X., 2008, Magnetic reduction-to-the-pole at low latitudes: Observations and considerations: The Leading Edge, **27**, 990–1002, doi: 10.1190/1.2967550.

Li, Y., and D. W. Oldenburg, 1996, 3-D inversion of magnetic data: Geophysics, **61**, 394–408, doi: 10.1190/1.1443968.

Li, Y., and D. W. Oldenburg, 2000, Joint inversion of surface and three-component borehole magnetic data: Geophysics, **65**, 540–552, doi: 10.1190/1.1444749.

Li, Y., and D. W. Oldenburg, 2003, Fast inversion of large-scale magnetic data using wavelet transforms and a logarithmic barrier method: Geophysical Journal International, **152**, 251–265, doi: 10.1046/j.1365-246X.2003.01766.x.

Losier, L., 1986, A Geophysical Viewpoint, *in* M. J. de Wit and L. D. Ashwal, eds., Workshop on Tectonic Evolution of Greenstone Belts, Lunar and Planetary Institute, 37.

Markwitz, V., K. A. A. Hein, M. W. Jessell, and J. Miller, 2016, Metallogenic portfolio of the West Africa craton: Ore Geology Reviews, **78**, 558–563, doi: 10.1016/j.oregeorev.2015.10.024.

Martin, R., V. Monteiller, D. Komatitsch, S. Perrouty, M. Jessell, S. Bonvalot, and M. Lindsay, 2013, Gravity inversion using wavelet-based compression on parallel hybrid CPU/GPU systems: application to southwest Ghana: Geophysical Journal International, **195**, 1594–1619, doi: 10.1093/gji/ggt334.

Martin, R., V. Ogarko, J. Giraud, B. Plazolles, P. Angrand, S. Rousse, and M. Macouin, 2025, Gravity data inversion of the Pyrenees range using Taguchi sensitivity analysis and ADMM bound constraints based on seismic data: Geophysical Journal International, **240**, 829–858, doi: 10.1093/gji/ggae410.

Martinez, C., Y. Li, R. Krahenbuhl, and M. A. Braga, 2013, 3D inversion of airborne gravity gradiometry data in mineral exploration: A case study in the Quadrilátero Ferrífero, Brazil: Geophysics, **78**, B1–B11, doi: 10.1190/geo2012-0106.1.

Masurel, Q., A. Eglinger, N. Thébaud, A. Allibone, A.-S. André-Mayer, H. McFarlane, J. Miller, M. Jessell, L. Aillères, O. Vanderhaeghe, S. Salvi, L. Baratoux, S. Perrouty, G. Begg, D. Fougerouse, P. Hayman, O. Wane, A. Tshibubudze, L. Parra-Avila, A. Kouamélan, and P. O.

Amponsah, 2022, Paleoproterozoic gold events in the southern West African Craton: review and synopsis: Mineralium Deposita, **57**, 513–537, doi: 10.1007/s00126-021-01052-5.

McCuaig, T. C., 2017, Exploration targeting across scales – where to from here? TARGET 2017, Geological Survey of Western Australia (GSWA), 103–106.

McFarlane, H. B., L. Ailleres, P. Betts, J. Ganne, L. Baratoux, M. W. Jessell, and S. Block, 2019, Episodic collisional orogenesis and lower crust exhumation during the Palaeoproterozoic Eburnean Orogeny: Evidence from the Sefwi Greenstone Belt, West African Craton: Precambrian Research, **325**, 88–110, doi: 10.1016/j.precamres.2019.02.012.

Meng, Z., F. Li, W. Liu, and W. Li, 2024, Improvement of density inversion efficiency with projected gradient method: Application to FTG data: Journal of Applied Geophysics, **220**, 105276, doi: 10.1016/j.jappgeo.2023.105276.

Mériaud, N., 2020, Litho-tectonic evolution and metallogeny of the Yaouré gold camp, Côte d'Ivoire West Africa; Integration into the southern West African craton evolution: PhD Thesis, The University of Western Australia.

Mériaud, N., Q. Masurel, N. Thébaud, and G. Tourigny, 2022, Fluid pressure–dominated orogenic gold mineralization under low differential stress: case of the Yaouré gold camp, Côte d'Ivoire, West Africa: Mineralium Deposita, **57**, 539–556, doi: 10.1007/s00126-019-00927-y.

Mériaud, N., N. Thébaud, Q. Masurel, P. Hayman, M. Jessell, A. Kemp, N. J. Evans, C. M. Fisher, and P. M. Scott, 2020, Lithostratigraphic evolution of the Bandamian Volcanic Cycle in central Côte d'Ivoire: Insights into the late Eburnean magmatic resurgence and its geodynamic implications: Precambrian Research, **347**, 1–22, doi: 10.1016/j.precamres.2020.105847.

Milsom, J., and A. Eriksen, 2011, Field Geophysics, 4th ed.: Wiley.

Moore, J. G., 2001, Density of basalt core from Hilo drill hole, Hawaii: Journal of Volcanology and Geothermal Research, **112**, 221–230, doi: 10.1016/S0377-0273(01)00242-6.

Nettleton, L. L., 1962, Gravity and Magnetics for Geologists and Seismologists: AAPG Bulletin, **46**, 1815–1838, doi: 10.1306/BC7438F3-16BE-11D7-8645000102C1865D.

Ngom, N. M., M. Mbaye, D. Baratoux, L. Baratoux, K. E. Ahoussi, J. K. Kouame, G. Faye, and E. H. Sow, 2022, Recent expansion of artisanal gold mining along the Bandama River (Côte d'Ivoire): International Journal of Applied Earth Observation and Geoinformation, **112**, 102873, doi: 10.1016/j.jag.2022.102873.

Nitzsche, T., C. Rolf, and H. de Wall, 2006, Origin of magnetic anomalies in volcaniclastic units of the Messel maar-diatreme (Germany): Zeitschrift Der Deutschen Gesellschaft Für Geowissenschaften, 373–385, doi: 10.1127/1860-1804/2006/0157-0373.

Ogarko, V., J. Giraud, R. Martin, and M. Jessell, 2021, Disjoint interval bound constraints using the alternating direction method of multipliers for geologically constrained inversion: Application to gravity data: Geophysics, **86**, G1–G11, doi: 10.1190/geo2019-0633.1.

Ogarko, V., K. Frankcombe, T. Liu, J. Giraud, R. Martin, and M. Jessell, 2024, Tomofast-x 2.0: an open-source parallel code for inversion of potential field data with topography using wavelet compression: Geoscientific Model Development, **17**, 2325–2345, doi: 10.5194/gmd-17-2325-2024.

Oldenburg, D. W., and D. A. Pratt, 2017, Geophysical Inversion for Mineral Exploration: a Decade of Progress in Theory and Practice: Exploration 17: 6th Decennial Mineral Exploration Conference, Proceedings, 1–37.

Paoletti, V., M. Fedi, F. Italiano, G. Florio, and S. Ialongo, 2016, Inversion of gravity gradient tensor data: does it provide better resolution? Geophysical Journal International, **205**, 192–202, doi: 10.1093/gji/ggw003.

Perret, J., M. W. Jessell, Q. Masurel, P. C. Hayman, N. Thébaud, L. Baratoux, A. Kouamélan, A. Eglinger, A.-S. André-Mayer, A. Y. Koffi, I. Dia, J. Koné, J. Davis, O. Wane, P. O. Amponsah, S. Naba, and O. Vanderhaeghe, 2025, Review of Paleoproterozoic tectonics in the southern West African Craton: Insights from multi-disciplinary data integration: Precambrian Research, **422**, 107707, doi: 10.1016/j.precamres.2025.107707.

Perrouty, S., L. Aillères, M. W. Jessell, L. Baratoux, Y. Bourassa, and B. Crawford, 2012, Revised Eburnean geodynamic evolution of the gold-rich southern Ashanti Belt, Ghana, with new field and geophysical evidence of pre-Tarkwaian deformations: Precambrian Research, **204–205**, 12–39, doi: 10.1016/j.precamres.2012.01.003.

Pilkington, M., 2014, Evaluating the utility of gravity gradient tensor components: Geophysics, **79**, G1–G14.

Pouclet, A., S. Doumbia, and M. Vidal, 2006, Geodynamic setting of the Birimian volcanism in central Ivory Coast (western Africa) and its place in the Palaeoproterozoic evolution of the Man Shield: Bulletin de La Société Géologique de France, **177**, 105–121, doi: 10.2113/gssgfbull.177.2.105.

Ralph, A., and D. Saunders, 2023, Yaouré Gold Mine – Côte d'Ivoire: Technical Report, Perseus Mining Limited, https://perseusmining.com/storage/2023/12/2023-Yaoure-Gold-Mine-Technical-Report_231218_Final.pdf.

Rashidifard, M., J. Giraud, M. Lindsay, and M. Jessell, 2024, Cooperative geophysical inversion integrated with 3D geological modelling in the Boulia region, QLD: Geophysical Journal International, **238**, 860–880, doi: 10.1093/gji/ggae179.

Ridley, J., 2013, Ore Deposit Geology: Cambridge University Press.

Schön, J. H., 2015, Magnetic Properties, *in* J. H. Schön, ed., Developments in Petroleum Science 65: Physical Properties of Rocks, Elsevier, 415–435.

Seequent Limited, 2023, Oasis Montaj Educational version 2023.2 (20231121.28).

Silvennoinen, H., and E. Kozlovskaya, 2007, 3D structure and physical properties of the Kuhmo Greenstone Belt (eastern Finland): Constraints from gravity modelling and seismic data and implications for the tectonic setting: Journal of Geodynamics, **43**, 358–373, doi: 10.1016/j.jog.2006.09.018.

Stettler, E. H., J. H. de Beer, D. Eberle, J. Ludden, and M. Mareschal, 1997, Geophysics and Deep Structures, *in* M. J. de Wit and L. D. Ashwal, eds., Greenstone Belts, Oxford Monograph on Geology and Geophysics, Clarendon Press, 339–375.

Subrahmanyam, M., and T. K. S. P. Rao, 2009, Interpretation of magnetic anomalies using some simple characteristic positions over tabular bodies: Exploration Geophysics, **40**, 265–276, doi: 10.1071/EG09005.

Swain, C. J., 1976, A FORTRAN IV program for interpolating irregularly spaced data using the difference equations for minimum curvature: Computers & Geosciences, **1**, 231–240, doi: 10.1016/0098-3004(76)90071-6.

Temnikova, E. Y., D. K. Potter, and A. Ali, 2025, Assessing Magnetic Methods for Estimating Mineral Content of Rocks in Northern Alberta: SPWLA 66th Annual Logging Symposium, OnePetro, Expanded Abstracts, 1–12, doi: 10.30632/SPWLA-2025-0026.

de la Varga, M., A. Schaaf, and F. Wellmann, 2019, GemPy 1.0: open-source stochastic geological modeling and inversion: Geoscientific Model Development, **12**, 1–32, doi: 10.5194/gmd-12-1-2019.

Wang, G., Y. Zhu, S. Zhang, C. Yan, Y. Song, Z. Ma, D. Hong, and T. Chen, 2012, 3D geological modeling based on gravitational and magnetic data inversion in the Luanchuan ore region, Henan Province, China: Journal of Applied Geophysics, **80**, 1–11, doi: 10.1016/j.jappgeo.2012.01.006.

Weber, F., F. Gauthier-Lafaye, H. Whitechurch, M. Ulrich, and A. El Albani, 2016, The 2-Ga Eburnean Orogeny in Gabon and the opening of the Francevillian intracratonic basins: A review: Comptes Rendus Geoscience, **348**, 572–586, doi: 10.1016/j.crte.2016.07.003.

Webring, M. W., 1981, MINC: a gridding program based on minimum curvature: Report 81-1224, USGS, https://pubs.usgs.gov/of/1981/1224/report.pdf.

Wellmann, F., and G. Caumon, 2018, 3-D Structural geological models: Concepts, methods, and uncertainties, *in* C. Schmelzbach, ed., Advances in Geophysics, Elsevier, 1–121.

Williams, N. C., 2008, Geologically-constrained UBC–GIF gravity and magnetic inversions with examples from the Agnew-Wiluna greenstone belt, Western Australia: PhD Thesis, The University of British Columbia.

LIST OF FIGURES

Figure 1. (a) Geological map of the Bouaflé Greenstone Belt with the location of the Yaouré Greenstone Belt (given by the geophysical survey area). KB and TB stand for Koudougou-Benou Tokorossou-Benou, respectively. (b) Available stratigraphic column for the Yaouré gold mine region only. Note no equivalent column exists for the study area. Modified from Mériaud et al. (2020, 2022).

Figure 2. Digital terrain model (DTM) with faults (red lines), geological units (black contours), and the Yaouré mine location (black hexagon) overlaid from Figure 1a.

Figure 3. Total magnetic anomaly (TMA) overlaid with faults (red lines), geological units (black contours), and the Yaouré mine location (black hexagon) from Figure 1a. A continuous color ramp with linear color stretch was applied for visualization. Note that the color bar was shifted so that zero corresponds to white.

Figure 4. FTGG grids (gray outline) and their derived grids, T_z (green outline) and T_z Residual (T_z Res, orange outline) shown with the geological structures from Figure 1a.

Figure 5. Isosurfaces of the inverted models derived from the main geophysical data: (a) TMA, (b) tensor components of the FTGG data, (c) T_z, and (d) T_z residual (T_z Res), all overlaid with the geological map features of Figure 1a. Blue isosurfaces represent the 2.5th percentile values, while red isosurfaces represent the 97.5th percentile values of the respective density models (b), (c) and (d). The isosurfaces of the magnetic susceptibility model (a) correspond to a value slightly above the 97.5th percentile. The blue polygon in the inverted models outlines the geophysical survey area. Models were clipped to the survey boundaries. Figures (e) and (f) show normalized histogram curves indicating the mean (μ) and standard deviation (σ) of each data set.

Note that x-axis in (e) is in logarithmic scale, while in (f) each colored mean and standard deviations value corresponds to the respective line in the plot.

Figure 6. Cross sections of the inverted models perpendicular to the KB fault, derived respectively from the TMA (first row), FTGG components (second row), T_z (third row), and T_z residual (last row) data sets, alongside profiles from geological map of Figure 1a. Each slice displays ten linear contour levels. White areas represent value equal to the background density in the inverted models for density. KB stands for Koudougou-Benou and TB for Tokorossou-Benou. Yellow lines within the slices represent the dip direction and dip angle (with uncertainty added) of anomalies measured in the susceptibility model.

Figure 7. Cross sections of the inverted models perpendicular to the TB fault, derived respectively from the TMA (first row), FTGG components (second row), T_z (third row), and T_z residual (last row) data sets, alongside profiles from geological map of Figure 1a. Each slice displays ten linear contour levels. White areas represent value equal to the background density in the inverted models for density. KB stands for Koudougou-Benou and TB for Tokorossou-Benou. Yellow lines within the slices represent the dip direction and dip angle (with uncertainty added) of anomalies measured in the susceptibility model.

Figure 8. Cross sections of the inverted models of significant geological features, derived respectively from the TMA (first row), FTGG components (second row), T_z (third row), and T_z residual (last row) data sets, alongside profiles from geological map of Figure 1a. Each slice displays ten linear contour levels. White areas represent value equal to the background density in the inverted models for density. Figure (f) was trimmed to show data between 2.5th and 97.5th percentile. KB stands for Koudougou-Benou and TB for Tokorossou-Benou. Yellow lines within

the slices represent the dip direction and dip angle (with uncertainty added) of anomalies measured in the susceptibility model.

Figure 9. Geological map with the orientation of magnetic susceptibilities derived from slices measurements of Figures 6, 7, and 8. The dip angle symbol follows the conventional structural geology format, i.e., the long horizontal line shows the strike, the short line indicates the dip direction, and the accompanying number the dip angle in degrees.

Figure A-1. Observed, calculated and data misfit for inversions using TMA, T_z and T_z residual (Tz Res) data, overlain by geological contacts and structures from the geological map (see Figure 4 for the legend). Note that the color bar in the data misfit grids was shifted so that it corresponds to a white zero value.

Figure A-2. Observed, calculated and data misfit for the six components used in inversion of FTGG data, overlain by geological contacts and structures from the geological map (see Figure 4 for the legend). Note that the color bar in the data misfit grids was shifted so that it corresponds to a white zero value.

LIST OF TABLES

Table 1. Airborne survey specifications.

Table 2. Ranking of magnetic susceptibility and density contrast for the geological units discussed in this study. Ranks decrease from 1 (highest values) to 6 (lowest) within each property. Units with overlapping or indistinguishable physical properties were grouped together in an arbitrary order within the same rank.

Table A-1. Maximum RAM usage and runtime for the inversions discussed in this study, along with the reconstruction error of the compressed sensitivity matrices for each inversion. All inversions ran using 36 processors.

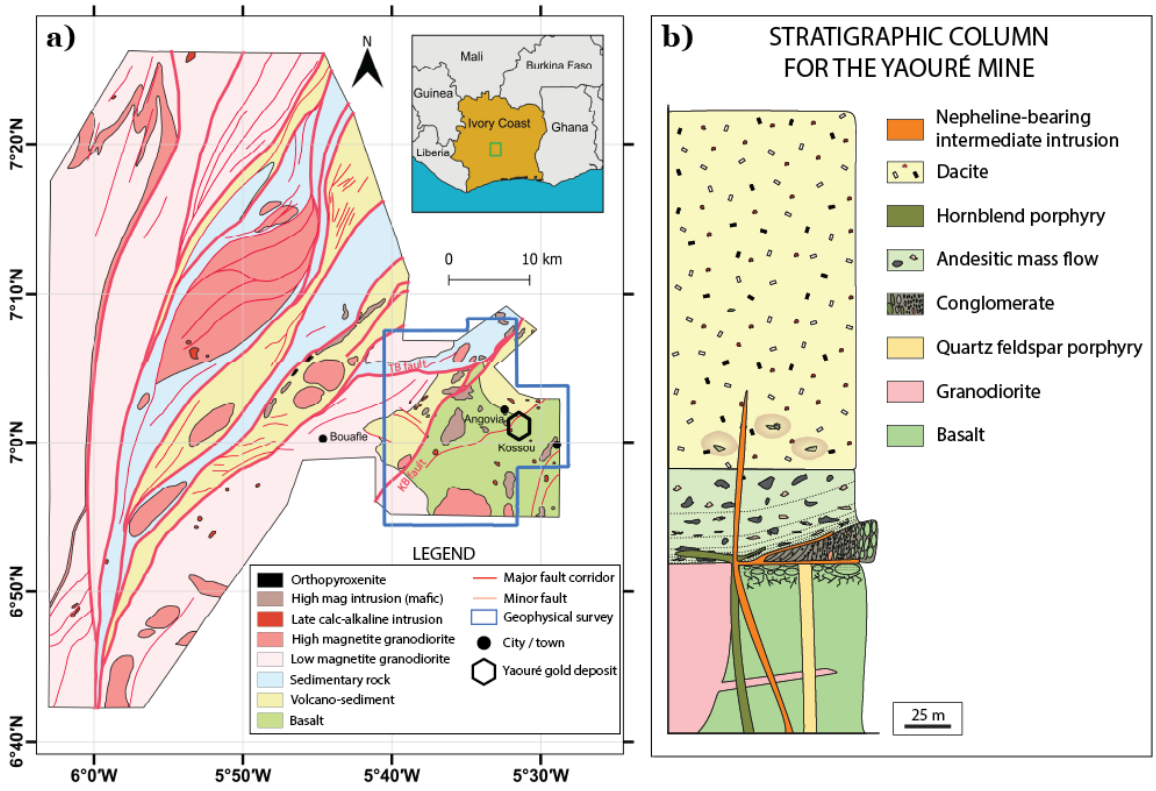


Figure 1. (a) Geological map of the Bouaflé Greenstone Belt with the location of the Yaouré Greenstone Belt (given by the geophysical survey area). KB and TB stand for Koudougou-Benou Tokorossou-Benou, respectively. (b) Available stratigraphic column for the Yaouré gold mine region only. Note no equivalent column exists for the study area. Modified from Mériaud et al. (2020, 2022).

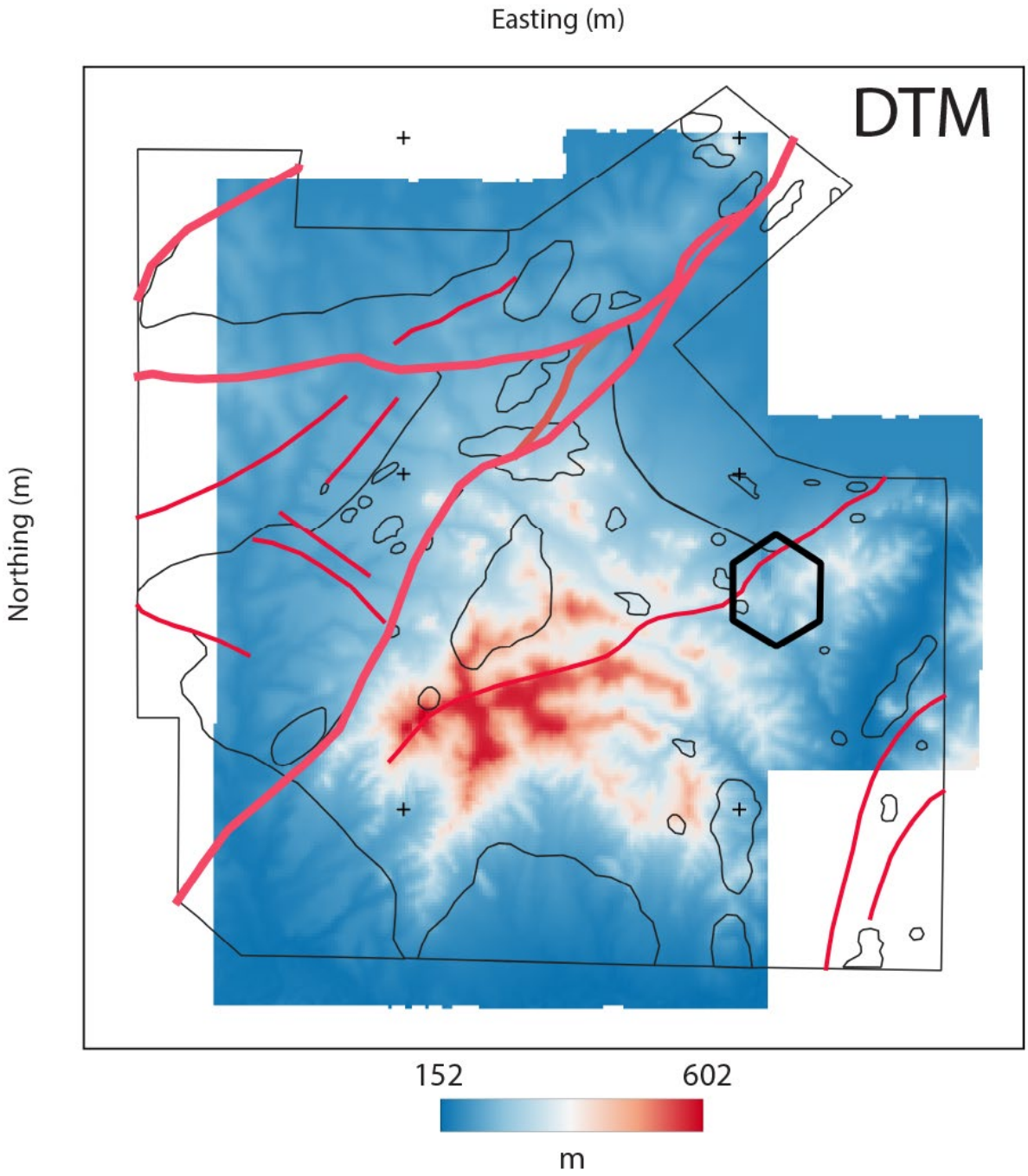


Figure 2. Digital terrain model (DTM) with faults (red lines), geological units (black contours), and the Yaouré mine location (black hexagon) overlaid from Figure 1a.

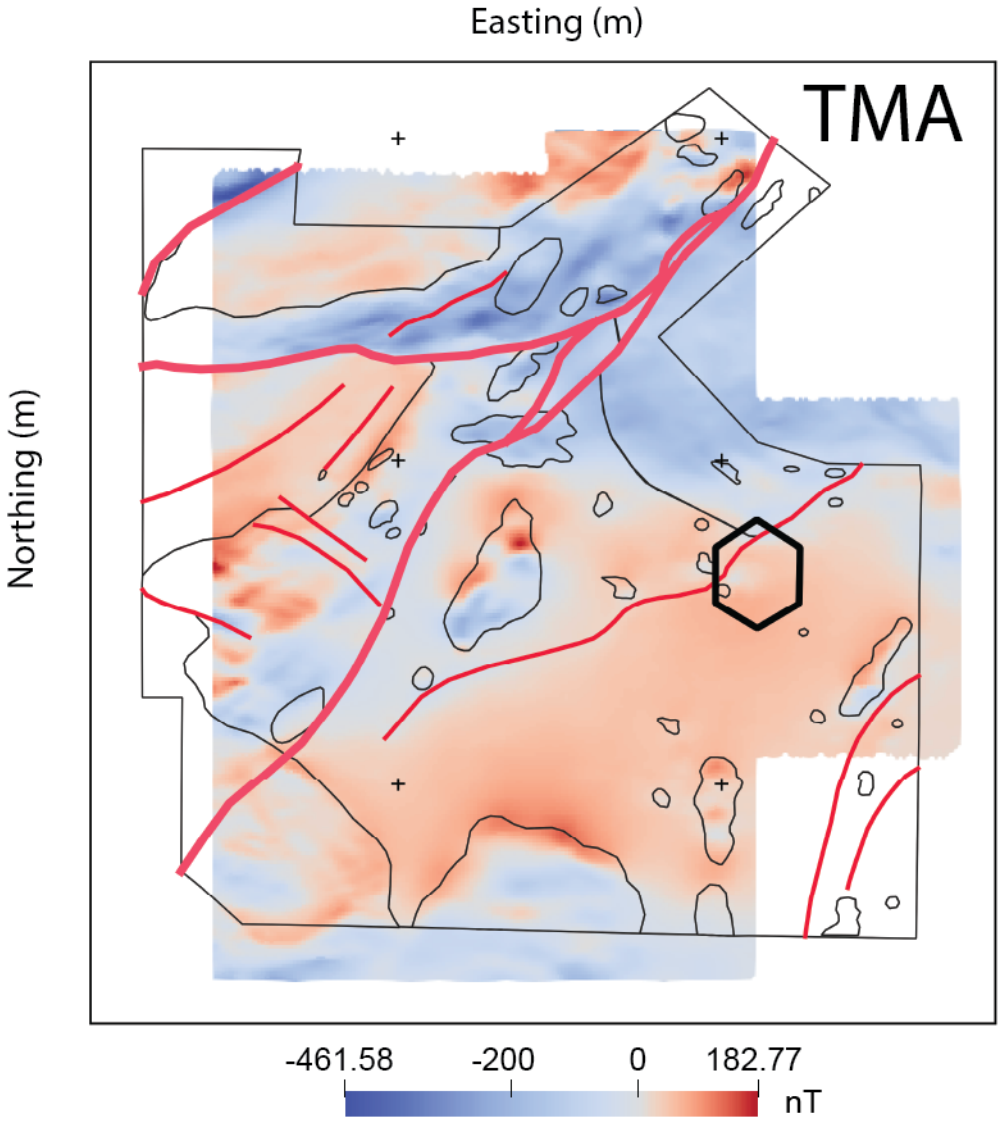


Figure 3. Total magnetic anomaly (TMA) overlaid with faults (red lines), geological units (black contours), and the Yaouré mine location (black hexagon) from Figure 1a. A continuous color ramp with linear color stretch was applied for visualization. Note that the color bar was shifted so that zero corresponds to white.

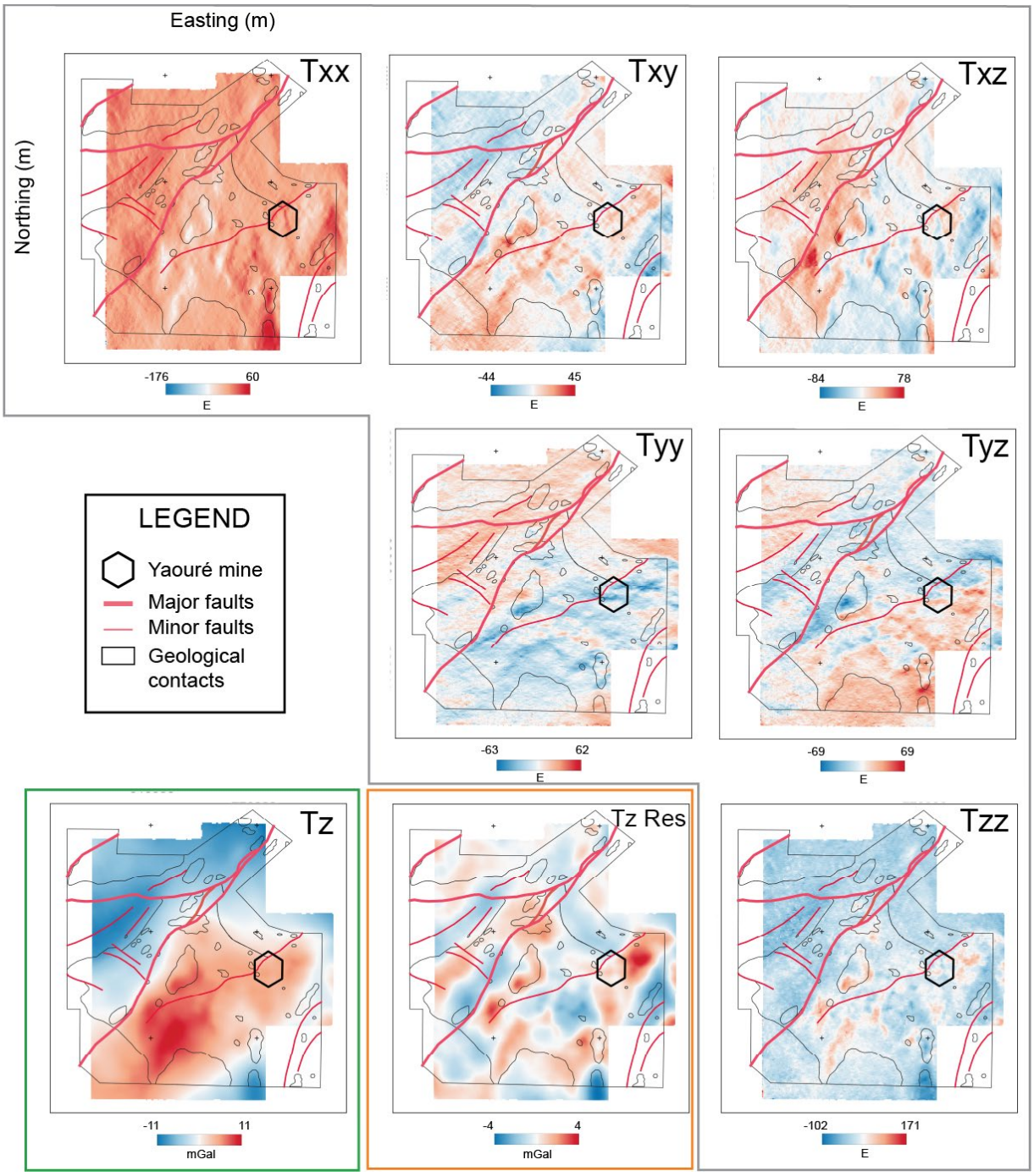


Figure 4. FTGG grids (gray outline) and their derived grids, T_z (green outline) and T_z Residual (T_z Res, orange outline) shown with the geological structures from Figure 1a.

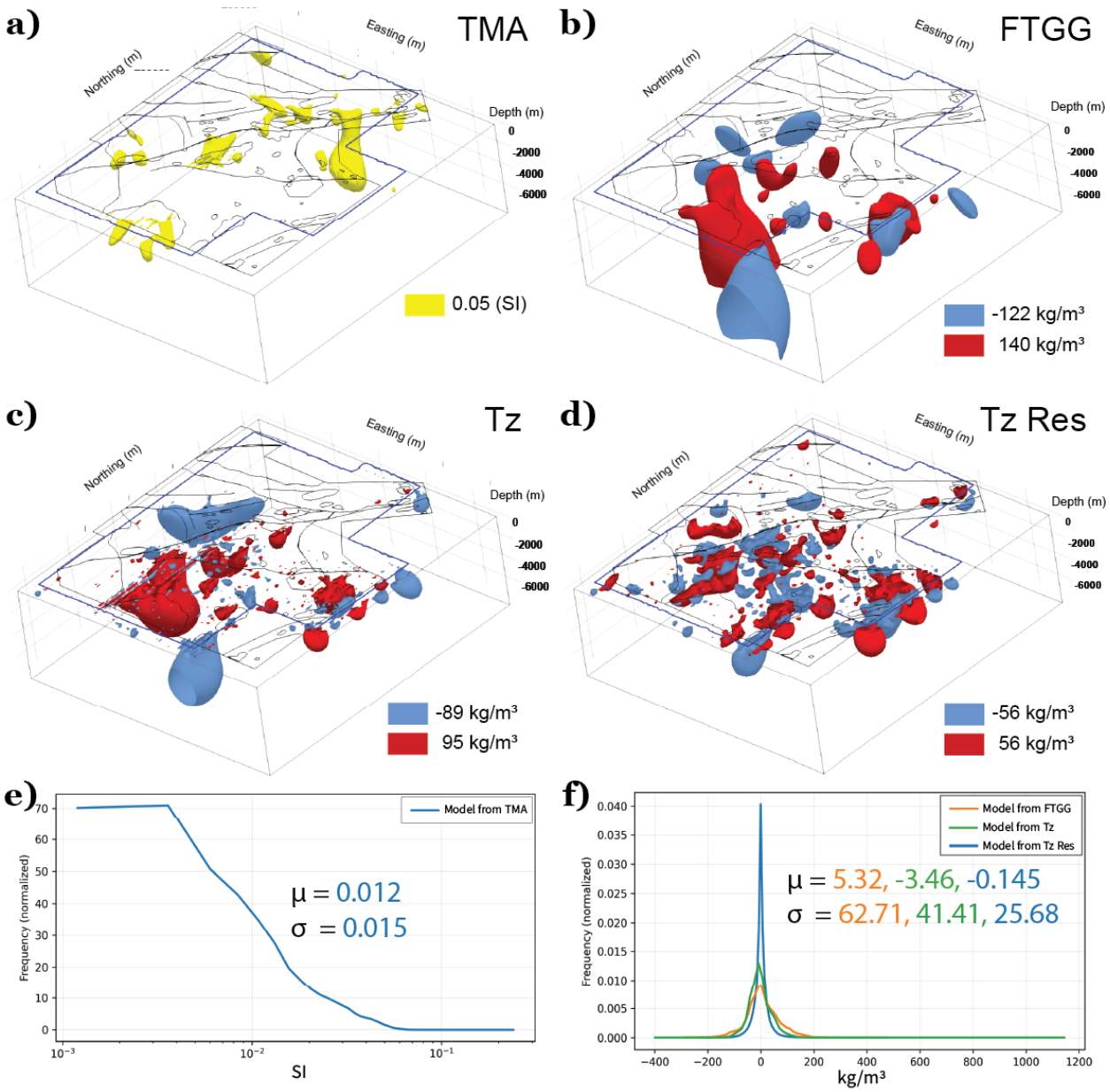


Figure 5. Isosurfaces of the inverted models derived from the main geophysical data: (a) TMA, (b) tensor components of the FTGG data, (c) T_z, and (d) T_z residual (T_z Res), all overlaid with the geological map features of Figure 1a. Blue isosurfaces represent the 2.5th percentile values, while red isosurfaces represent the 97.5th percentile values of the respective density models (b), (c) and (d). The isosurfaces of the magnetic susceptibility model (a) correspond to a value slightly above the 97.5th percentile. The blue polygon in the inverted models outlines the geophysical survey area. Models were clipped to the survey boundaries. Figures (e) and (f) show normalized histogram curves indicating the mean (μ) and standard deviation (σ) of each data set. Note that x-axis in (e) is in logarithmic scale, while in (f) each colored mean and standard deviations value corresponds to the respective line in the plot.

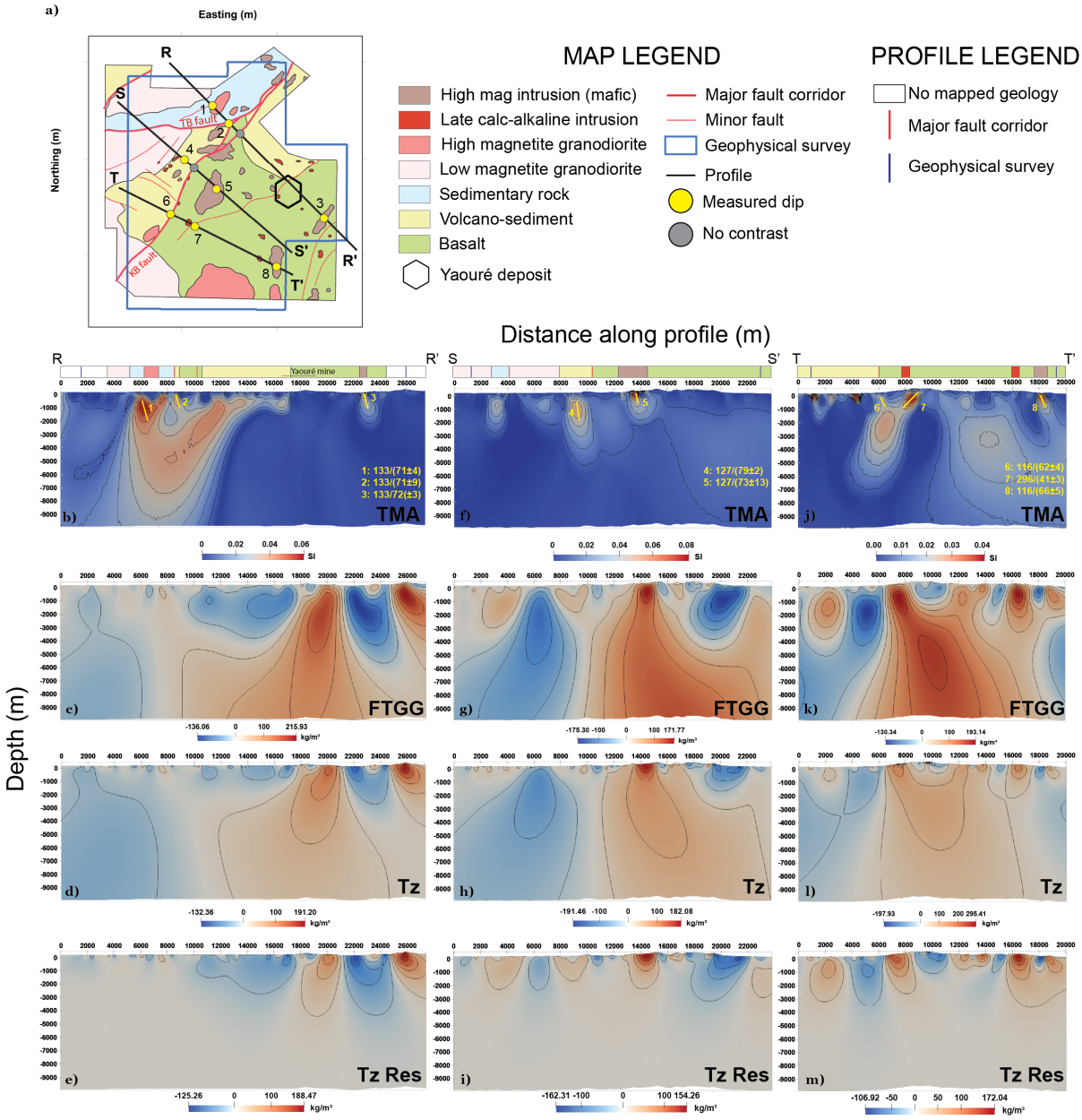


Figure 6. Cross sections of the inverted models perpendicular to the KB fault, derived respectively from the TMA (first row), FTGG components (second row), T_z (third row), and T_z residual (last row) data sets, alongside profiles from geological map of Figure 1a. Each slice displays ten linear contour levels. White areas represent value equal to the background density in the inverted models for density. KB stands for Koudougou-Benou and TB for Tokorossou-Benou. Yellow lines within the slices represent the dip direction and dip angle (with uncertainty added) of anomalies measured in the susceptibility model.

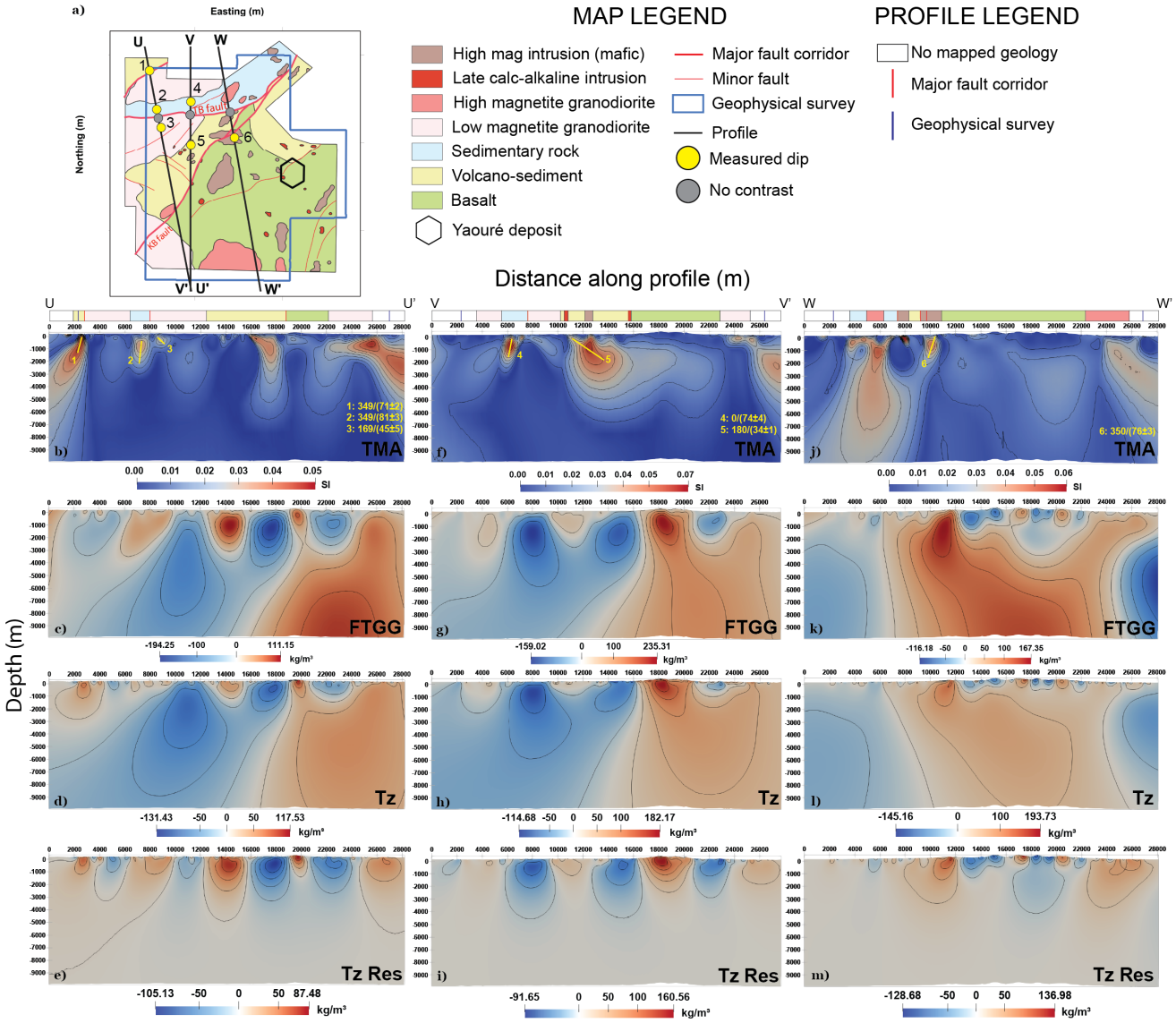


Figure 7. Cross sections of the inverted models perpendicular to the TB fault, derived respectively from the TMA (first row), FTGG components (second row), T_z (third row), and T_z residual (last row) data sets, alongside profiles from geological map of Figure 1a. Each slice displays ten linear contour levels. White areas represent value equal to the background density in the inverted models for density. KB stands for Koudougou-Benou and TB for Tokorossou-Benou. Yellow lines within the slices represent the dip direction and dip angle (with uncertainty added) of anomalies measured in the susceptibility model.

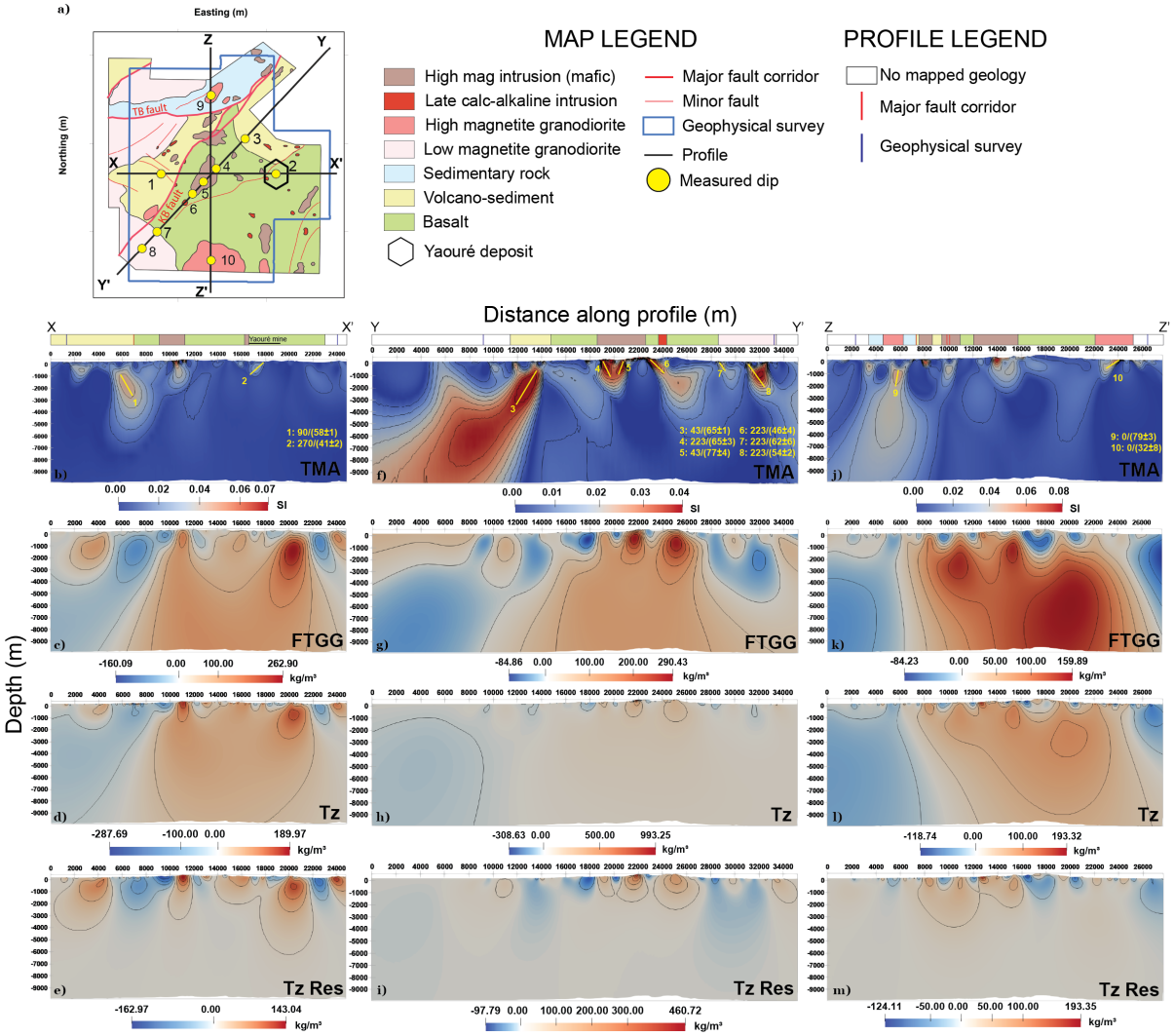


Figure 8. Cross sections of the inverted models of significant geological features, derived respectively from the TMA (first row), FTGG components (second row), T_z (third row), and T_z residual (last row) data sets, alongside profiles from geological map of Figure 1a. Each slice displays ten linear contour levels. White areas represent value equal to the background density in the inverted models for density. Figure (f) was trimmed to show data between 2.5th and 97.5th percentile. KB stands for Koudougou-Benou and TB for Tokorossou-Benou. Yellow lines within the slices represent the dip direction and dip angle (with uncertainty added) of anomalies measured in the susceptibility model.

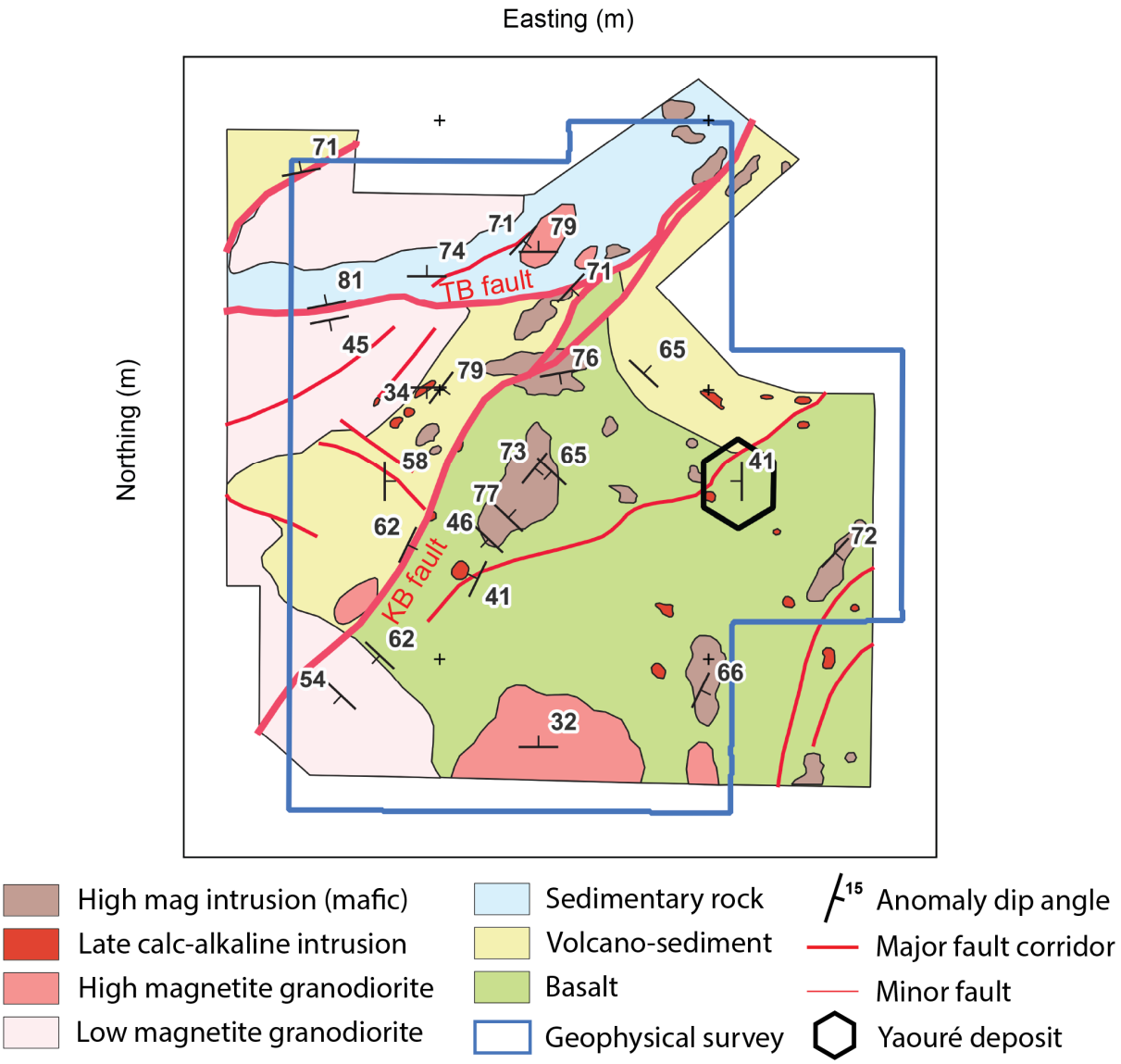


Figure 9. Geological map with the orientation of magnetic susceptibilities derived from slices measurements of Figures 6, 7, and 8. The dip angle symbol follows the conventional structural geology format, i.e., the long horizontal line shows the strike, the short line indicates the dip direction, and the accompanying number the dip angle in degrees.

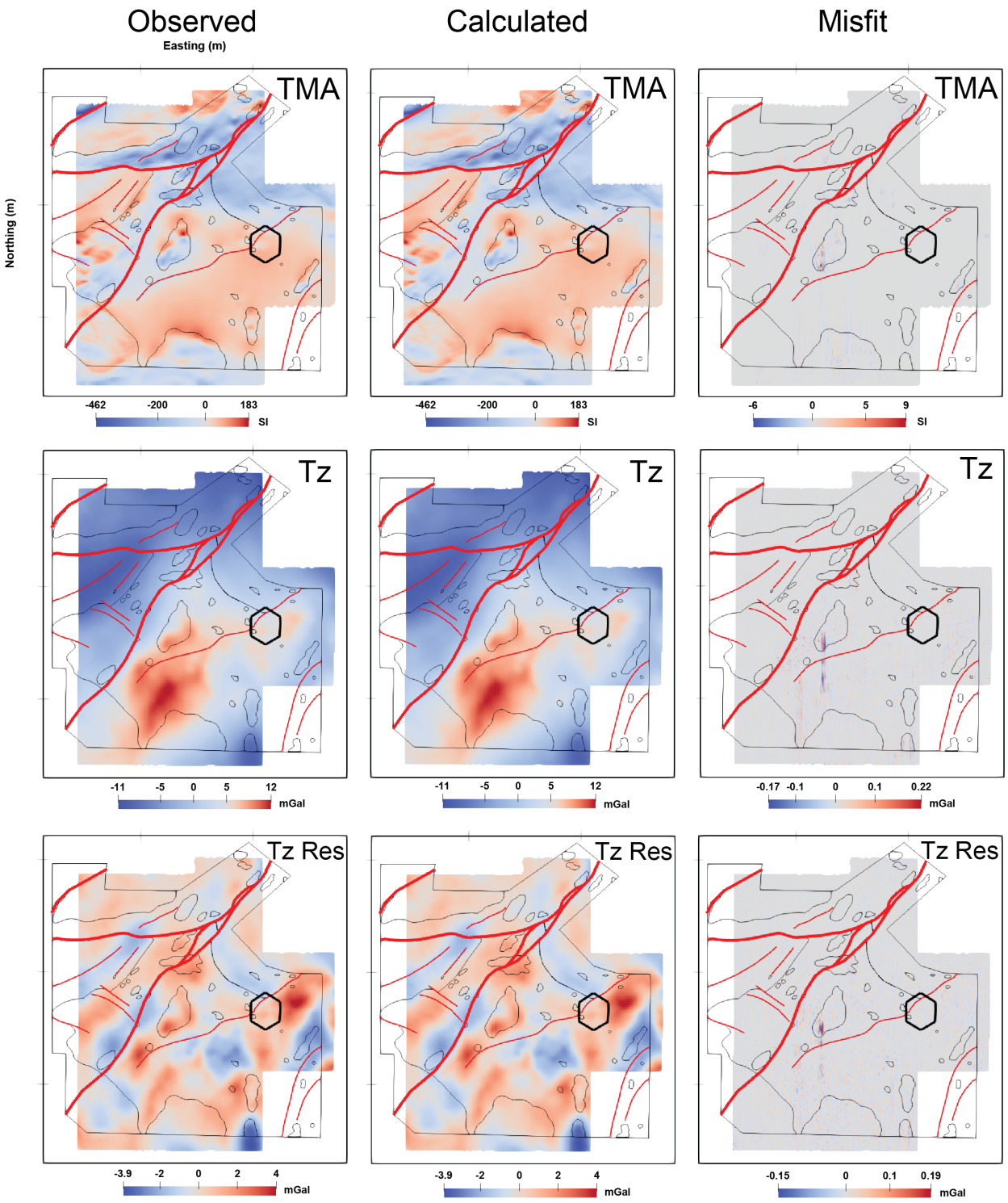


Figure A-1. Observed, calculated and data misfit for inversions using TMA, T_z and T_z residual (Tz Res) data, overlain by geological contacts and structures from the geological map (see Figure 4 for the legend). Note that the color bar in the data misfit grids was shifted so that it corresponds to a white zero value.

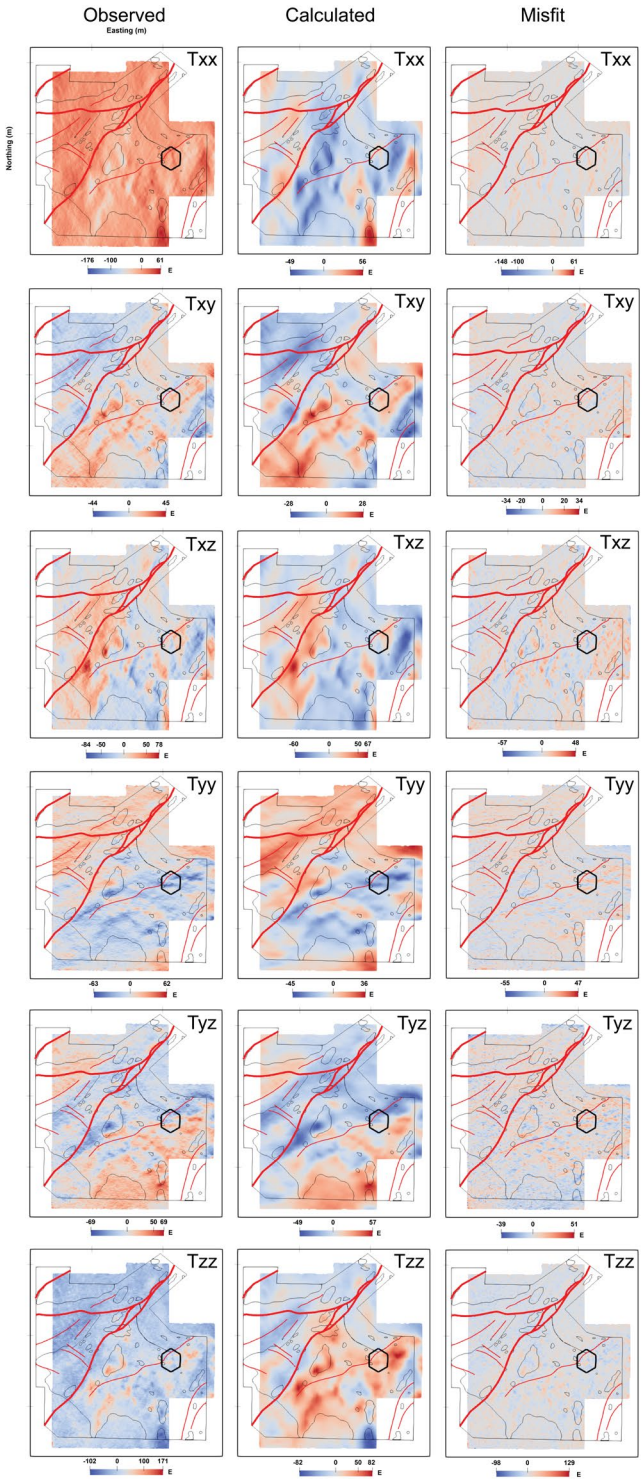


Figure A-2. Observed, calculated and data misfit for the six components used in inversion of FTGG data, overlain by geological contacts and structures from the geological map (see Figure 4 for the legend). Note that the color bar in the data misfit grids was shifted so that it corresponds to a white zero value.

Table 1. Airborne survey specifications.

Airborne gravity gradiometer	Lockheed Martin FTG 3
Airborne magnetometer	Geometrics G-822 mobile cesium magnetometer
Approximate sample spacing for FTGG	60 m
Approximate sample spacing for magnetics	6 m
Nominal in-line orientation (azimuth)	0.3588º / 180.3588º
Final total survey length	4,707 km
Coordinate reference system	Universal Transverse Mercator (UTM) Zone 30 N
Horizontal datum	World Geodetic System 1984 (WGS 84)
Vertical datum	Earth Gravitation Model 1996 (EGM 96)

Table 2. Ranking of magnetic susceptibility and density contrast for the geological units discussed in this study. Ranks decrease from 1 (highest values) to 6 (lowest) within each property. Units with overlapping or indistinguishable physical properties were grouped together in an arbitrary order within the same rank.

Rank	**Magnetic susceptibility**	**Density contrast**
1	High mag intrusion (mafic)	High mag intrusion (mafic)
2	Sedimentary rock	Late calc-alkaline intrusion, Basalt
3	High magnetite granodiorite	High magnetite granodiorite, Volcano-sedimentary, Sedimentary rock
4	Volcano-sedimentary	Low magnetite granodiorite
5	Low magnetite granodiorite	-
6	Basalt, Late calc-alkaline intrusion	-

Table A-1. Maximum RAM usage and runtime for the inversions discussed in this study, along with the reconstruction error of the compressed sensitivity matrices for each inversion. All inversions ran using 36 processors.

Derived data used in inversion	**RAM usage (GB)**	**Runtime**	**Reconstruction error ($\times 10^{-4}$)**
TMA	59.80	1h 39m 37s	6.34
FTGG	333.98	3h 02m 33s	6.07
Tz	57.81	52m 21.52s	7.36
Tz Residual	57.73	54m 22.74s	7.36